nature communications

Article

https://doi.org/10.1038/s41467-024-51726-7

ZmGDIα-hel counters the RBSDV-induced reduction of active gibberellins to alleviate maize rough dwarf virus disease

Received: 10 November 2023

Accepted: 15 August 2024

Published online: 31 August 2024

Check for updates

Suining Deng[1], Siqi Jiang[1], Baoshen Liu[2], Tao Zhong[1], Qingcai Liu[1], Jianju Liu[1], Yuanliang Liu[1], Can Yin[3], Chen Sun[3] & Mingliang Xu[1]

Maize rough dwarf disease (MRDD) threatens maize production globally. The P7-1 effector of the rice black-streaked dwarf virus (RBSDV) targets maize Rab GDP dissociation inhibitor alpha (ZmGDIα) to cause MRDD. However, P7-1 has difficulty recruiting a ZmGDIα variant with an alternative *helitron*-derived exon 10 (ZmGDIα-hel), resulting in recessive resistance. Here, we demonstrate that P7-1 can recruit another maize protein, gibberellin 2-oxidase 13 (ZmGA2ox7.3), which also exhibits tighter binding affinity for ZmGDIα than ZmGDIα-hel. The oligomerization of ZmGA2ox7.3 is vital for its function in converting bioactive gibberellins into inactive forms. Moreover, the enzymatic activity of ZmGA2ox7.3 oligomers increases when forming hetero-oligomers with P7-1/ZmGDIα, but decreases when ZmGDIα-hel replaces ZmGDIα. Viral infection significantly promotes ZmGA2ox7.3 expression and oligomerization in *ZmGDIα*-containing susceptible maize, resulting in reduced bioactive GA_1/GA_4 levels. This causes an auxin/cytokinin imbalance and ultimately manifests as MRDD syndrome. Conversely, in resistant maize, *ZmGDIα-hel* counters these virus-induced changes, thereby mitigating MRDD severity.

Plant viruses, primarily transmitted by biotic vectors, pose a significant threat to global food security by inflicting substantial damage to crops[1]. To combat viral infections, plants have evolved multiple layers of defense responses, which are collectively referred to as active resistance[2]. In addition, plants have developed passive resistance strategies, enabling them to evade viral recognition or exploitation by modifying or eliminating susceptibility factors, also referred to as recessive resistance[3]. Most of the naturally-occurring recessive resistance genes are related to the translation initiation factors eIF4E and eIF4G or their homologs[4]. Other loss-of-susceptibility genes include *ZmGDIα-hel*, *cPGK2*, *HvPDIL5-1*, and among others[5–7].

Maize rough dwarf disease (MRDD) is a devastating viral disease, often referred to as the "cancer" of maize. It was first reported in the late 1940s in northern Italy and subsequently spread to countries such as Greece, France, and Israel[8]. MRDD is caused by various *Fijivirus* pathogens in the family *Reoviridae*, among which the maize rough dwarf virus was detected in Europe, Mal de Río Cuarto virus was reported in South America, and the major pathogen responsible in East Asia is the rice black-streaked dwarf virus (RBSDV)[9,10]. RBSDV is transmitted to maize in a persistent manner by the small brown planthopper (*Laodelphax striatellus*)[11]. The typical symptoms of MRDD are characterized by severe growth abnormalities, including dwarfism, shortened internodes, abnormal ears/tassels, dark-green leaves, and white waxy enations on the backs of leaf veins[12]. RBSDV has a genome of 10 double-stranded RNAs (S1–S10), with sizes ranging from 1.8 to 4.5 kb[13,14]. Each segment encodes one or, in the case of S5, S7, and S9, two proteins[13]. Notably, the P7-1 effector, encoded by *S7-1*, forms tubular structures in RBSDV-infected plants and localizes to

[1]State Key Laboratory of Plant Environmental Resilience/College of Agronomy and Biotechnology/National Maize Improvement Center/Center for Crop Functional Genomics and Molecular Breeding, China Agricultural University, Beijing 100193, PR China. [2]College of Agronomy/State Key Laboratory of Crop Biology, Shandong Agricultural University, Taian 271018, PR China. [3]College of Agronomy and Biotechnology, China Agricultural University, Beijing 100193, PR China. e-mail: mxu@cau.edu.cn

the plasmodesmata, which utilizes both the secretory pathway and actomyosin motility system for intracellular virus transport and movement[15,16].

Phytohormones regulate plant growth, development, and stress responses[17,18]. Viral infections can disrupt the balance of phytohormones, leading to disease syndromes[17]. In *Arabidopsis*, the replicase protein of the *tomato mosaic virus* (TMV) interacts with Aux/IAA, disrupting the auxin response pathway to manifest symptoms[19]. In *rice dwarf virus* (RDV) disease, the P2 protein interacts with *ent*-kaurene oxidase to reduce rice GA_1 levels, resulting in a dwarf phenotype[20]. The P2 protein encoded by rice stripe virus interacts with and degrades rice OsNPR1, thereby disrupting the OsNPR1-mediated interplay between salicylic acid and jasmonic acid, ultimately facilitating viral infection[21]. In *Arabidopsis*, the geminivirus AC2/AL2 protein can interact with adenosine kinase and lead to an increase the expression of primary cytokinin-responsive genes[22]. Sw-5b, a plant leucine-rich repeat immune receptors (NLR), directly utilizes the ABA central regulator PP2C-SnRK2 complex to activate an ABA-dependent defense against viral pathogens[23].

Gibberellins (GAs) are a class of tetracyclic diterpenoid hormones that regulate plant stress responses, seed germination/dormancy, stem elongation, and leaf expansion[24]. In plants, GA_4 (a type of 13-H GAs), GA_1 (13-OH GA_4), GA_7 (another type of 13-H GAs), and GA_3 (13-OH GA_7) are considered major bioactive types[25]. Among these, GA_4 exhibits higher bioactivity than GA_1, and gibberellin 2-oxidases (GA2oxs) play a pivotal role in inactivating both GA_1 and GA_4[25–27]. GA2oxs are categorized into two groups, C_{19}-GA2oxs (also divided into class I and class II) and C_{20}-GA2oxs, based on their substrate specificity and enzymatic activity[26]. Overexpression of C_{19}-GA2oxs leads to a reduction of endogenous bioactive GAs, causing GA-deficient phenotypes[26,28].

In our previous work, we identified a *helitron*-induced variant *ZmGDIα-hel* that confers quantitative recessive resistance to MRDD by reducing disease severity index (DSI) by 24.2%–39.3%[5]. However, the detailed mechanism behind this resistance remains elusive. Specifically, we aim to understand how the interaction between the viral P7-1 effector and the host susceptibility factor (ZmGDIα) initiates MRDD and how the weaker interaction with ZmGDIα-hel alleviates MRDD? In this study, we identified a gibberellin 2-oxidase, ZmGA2ox7.3, as a key player in MRDD. During RBSDV infection, changes in the levels of ZmGA2ox7.3, ZmGDIα/ZmGDIα-hel, and P7-1, as well as their interactions, are crucial for modulating GA levels and, consequently, the balance of auxin/cytokinins. These factors ultimately determine the outcome of MRDD in maize.

Result

RBSDV-induced transcriptome reprogramming

In our previous study, we generated a pair of near-isogenic lines (NILs): the susceptible NIL-S (with the susceptibility allele, *ZmGDIα*) and the resistant NIL-R (with the resistance allele, *ZmGDIα-hel*)[5]. Following RBSDV infection, viral accumulation was detected in NIL-S starting from 16 days post inoculation (dpi) and increased linearly thereafter to reach a high level[5]. Consistent with this observation, we found that the viral *S10*, encoding the coat protein, exhibited dramatic accumulation in NIL-S but not in NIL-R (Fig. 1a). Similarly, the viral *S7-1* also showed significant accumulation (Fig. 1b). We performed RNA-seq analysis at 16 dpi between NIL-S and NIL-R. The differentially expressed genes (DEGs) were identified based on the criteria of fold-change > 2 and $P < 0.05$. Compared to NIL-R, NIL-S exhibited 24 downregulated and 21 upregulated DEGs (Fig. 1c, d). Gene Ontology (GO) term analysis revealed that these DEGs are mainly enriched in one molecular process: oxidoreductase activity, and in three biological processes: biology, oxidation-reduction, and single-organism (Supplementary Fig. 1a). KEGG analysis demonstrated significant DEG enrichment in three pathways: photosynthesis-antenna proteins, fatty acid elongation, and diterpenoid biosynthesis (Supplementary Fig. 1b).

Screening of potential P7-1 targets required for RBSDV infection

Four (*ZmGA2ox7.3*, *ZmDAO1*, *ZmB1B2*, and *ZmPPI1*) out of the 45 DEGs were captured in a previous Co-immunoprecipitation and mass spectrometry (Co-IP/MS) assay (Supplemental Table 1)[5]. Notably, the *ZmGA2ox7.3* gene (*Zm00001d039394*), encoding a gibberellin 2-oxidase 13, was dramatically upregulated in NIL-S compared to NIL-R (Fig. 1d, e). In the reverse transcription-quantitative real-time PCR (RT-qPCR) assay, *ZmGA2ox7.3* expression was significantly induced by RBSDV at 16 dpi in NIL-S, while it only showed a slight increase in NIL-R. However, no induction of *ZmGA2ox7.3* expression was observed in either NIL at 27 dpi (Fig. 1f). Regarding the other three DEGs, *ZmDAO1* (encoding a dioxygenase for auxin oxidation 1) exhibited downregulation in NIL-S in both RNA-seq and RT-qPCR analyses. *ZmB1B2* (encoding photosystem II light harvesting complex) and *ZmPPI1* (encoding peptidyl-prolyl cis-trans isomerase protein) showed no significant differential expression between the two NILs in the RT-qPCR, contrary to the RNA-seq data (Fig. 1d and Supplementary Fig. 1c, d). We further investigated potential interactions between these four proteins and ZmGDIα/ZmGDIα-hel using the bimolecular fluorescence complementation (BiFC) assay. ZmGA2ox7.3 showed a strong interaction with ZmGDIα but weaker with ZmGDIα-hel. In contrast, ZmDAO1 did not interact with either ZmGDIα or ZmGDIα-hel. ZmB1B2 exclusively interacted with ZmGDIα, and ZmPPI1 solely with ZmGDIα-hel (Supplementary Fig. 2a–e). All these findings were confirmed in the in vitro pull-down assays (Supplementary Fig. 2f and Fig. 4b).

A previous report in rice stated that the overexpression of gibberellin 2-oxidase genes resulted in stunted plants and shortened internodes[27,29], resembling typical MRDD symptoms. Combining expression patterns, protein-protein interaction profiles, and predicted functions, ZmGA2ox7.3 is likely another P7-1 target necessary for RBSDV infection.

Overexpression of *ZmGA2ox7.3* causes dwarf plant

We introduced an overexpression construct *pUbi:ZmGA2ox7.3-GFP* into the B73 recipient line, resulting in seven independent transgenic events. Compared to B73, the T_2 transgenic lines exhibited significantly enhanced expression of *ZmGA2ox7.3*, concomitant with plant dwarfism and internode shortening (Fig. 2a–e). The degree of internode shortening progressively intensified from the bottom to the top of the plant (Fig. 2f). When examining longitudinal sections of the uppermost internode, we observed that the average cell length in the T_2 transgenic lines was significantly shorter than in B73 (Fig. 2g, h). Subcellular localization using transient expression assays in *Nicotiana tabacum* leaves and maize protoplasts indicated that ZmGA2ox7.3 is localized to the plasma membrane, cytoplasm, and nucleus (Supplementary Fig. 2g, h).

To characterize ZmGA2ox7.3 further, we retrieved 24 GA2-oxidases in rice and maize from the NCBI public database (https://www.ncbi.nlm.nih.gov/) and MaizeGDB database (https://www.maizegdb.org/). Phylogenetic analysis revealed three distinct clades. ZmGA2ox7.3 shares its highest amino-acid identity with OsGA2ox7, followed by OsGA2ox3, in rice. These three proteins belong to the C_{19}-GA2oxs class I family, which functions to catalyze the conversion of biologically active GAs (GA_1 and GA_4) and their precursors (GA_9 and GA_{20}) into inactive GA forms (GA_8, GA_{34}, GA_{51}, and GA_{29}) (Supplementary Fig. 3a–c)[25,26]. This was exemplified by rice OsGA2ox3, which demonstrated its capability to catalyze the conversion of bioactive GA_4 into inactive GA_{34}[27].To ascertain whether ZmGA2ox7.3 belongs to the C_{19}-GA2oxs class I family, we tested it with three active gibberellins: GA_1, GA_3, and GA_4. Of them, GA_1 and GA_4 serve as typical substrates for GA2oxs. GA_3 is the product

https://doi.org/10.1038/s41467-024-51726-7

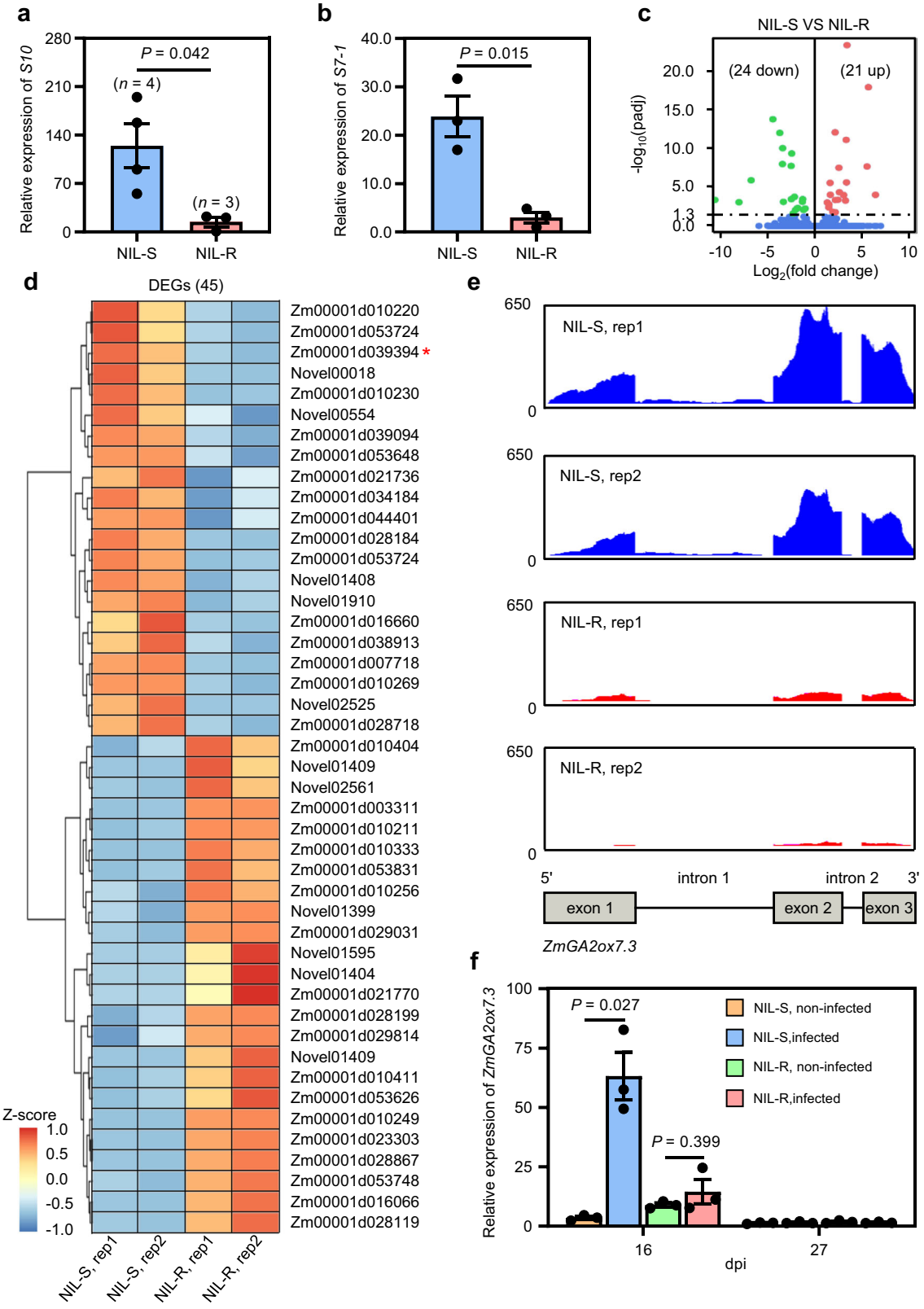

converted from GA_5, which in turn is derived from GA_{20}, and both conversions are catalyzed by GA3oxs[26]. We sprayed GA_1, GA_3, and GA_4 on B73 and its transgenic line overexpressing *ZmGA2ox7.3* at their seedling stages. B73 showed increased plant height upon spraying with these active GAs. Notably, the dwarf phenotype of the transgenic line could be fully restored with exogenous GA_3, while it was partially restored with GA_4 and to a lesser extent with GA_1 (Fig. 3a, b). In B73, all three active GAs significantly stimulated the expression of *ZmGA2ox7.3*; however, in the transgenic line, they all significantly lowered *ZmGA2ox7.3* expression (Fig. 3c). Additionally, GA_4 led to more accumulation of ZmGA2ox7.3 oligomers (Fig. 3d). These findings imply an inherent connection between ZmGA2ox7.3 and GA_4 or GA_1, consistent with the role of ZmGA2ox7.3 as a member of the C_{19}-GA2oxs family.

Fig. 1 | Transcriptome analysis of differentially expressed genes (DEGs) induced by RBSDV between the two NILs. a, **b** Relative expression of RBSDV *S10* and *S7-1* ($n = 3$) between the two NILs 16 days post RBSDV inoculation (dpi). A biological replicate in the NIL-R serves as a control sample for relative expression. **c** A volcano plot depicts the DEGs when comparing NIL-S to NIL-R at 16 dpi. Genes with significant down-regulation are represented by green dots, those with significant up-regulation by red dots, and those without significant change by blue dots. **d** A heatmap displays the 45 DEGs induced by RBSDV when comparing NIL-S to NIL-R. Red indicates up-regulation, while green denotes down-regulation. The red asterisk denotes ZmGA2ox7.3. **e** Enrichment of the *ZmGA2ox7.3* transcript in NIL-S compared to NIL-R. A structure diagram of *ZmGA2ox7.3* is provided at the bottom. **f** The relative expression of *ZmGA2ox7.3* was verified by RT-qPCR ($n = 3$). A biological replicate in the non-infected NIL-S at 27 dpi serve as a control sample for relative expression. In (**d**, **e**), "rep1" and "rep2" indicate two biological replicates. In (**a**, **b**, **f**), data are presented as means ± s.e.m. Significance was determined by a two-tailed Student's *t* test.

ZmGA2ox7.3 binds to ZmGDIα/P7-1 to form the hetero-oligomer

In split luciferase complementation (SLC) assays, luminescence signals were observed upon co-expression of *cLUC-ZmGA2ox7.3* with each of the three fusion genes (*ZmGDIα-nLUC*, *ZmGDIα-hel-nLUC*, and *P7-1-nLUC*) in *Nicotiana benthamiana* leaves (Fig. 4a). The co-immunoprecipitation (Co-IP) assay confirmed the associations of ZmGA2ox7.3 with each of the three proteins (Fig. 4b). The in vitro pull-down assay demonstrated that ZmGA2ox7.3 had a stronger interaction with ZmGDIα and P7-1, but only weaker with ZmGDIα-hel (Fig. 4c). The BiFC assay further confirmed that ZmGA2ox7.3 interacted more strongly with ZmGDIα and P7-1, and less so with ZmGDIα-hel (Fig. 4d).

We next conducted multiple SLC and micro-scale thermophoresis (MST) assays to precisely measure the binding strengths of ZmGA2ox7.3 with two ZmGDIα isoforms and P7-1. ZmGA2ox7.3 exhibited stronger luciferase (LUC) activity when interacting with ZmGDIα than with ZmGDIα-hel. Despite the lower quantity of P7-1, the interaction between ZmGA2ox7.3 and P7-1 also displayed strong LUC activity, albeit lower than that between ZmGA2ox7.3 and ZmGDIα (Supplementary Fig. 4a–f). MST assays definitely indicated that ZmGA2ox7.3 exhibits the highest affinity for P7-1, followed by ZmGDIα, and the lowest affinity for binding to ZmGDIα-hel (Supplementary Fig. 4g). To pinpoint the specific regions of ZmGDIα/ZmGDIα-hel that bind to ZmGA2ox7.3, we divided the *ZmGDIα* and *ZmGDIα-hel* cDNAs into multiple segments, as done in our previous study[5]. In SLC assays, ZmGA2ox7.3 demonstrated interactions with three segments of ZmGDIα, all of which included exon 10 (ZmGDIα$^{1\text{-}333}$, ZmGDIα$^{292\text{-}445}$, and ZmGDIα$^{292\text{-}333}$). This indicates the involvement of exon 10 in the interaction between ZmGA2ox7.3 and ZmGDIα (Supplementary Fig. 5a). Similarly, interactions between ZmGA2ox7.3 and three ZmGDIα-hel counterparts (ZmGDIα-hel$^{1\text{-}318}$, ZmGDIα-hel$^{292\text{-}430}$, and ZmGDIα-hel$^{292\text{-}318}$) were also observed, implying that the *helitron*-derived exon 10 did not completely abolish its ability to interact with ZmGA2ox7.3 (Supplementary Fig. 5b).

Our subsequent focus shifted to ascertain whether any other regions of ZmGDIα might also engaged in interactions with ZmGA2ox7.3. Intriguingly, both the N-terminus (ZmGDIα$^{1\text{-}291}$) and C-terminus (ZmGDIα$^{334\text{-}445}$) flanking exon 10 exhibited interactions with ZmGA2ox7.3 (Supplementary Fig. 5c). We then subdivided ZmGDIα$^{1\text{-}291}$ into two segments: ZmGDIα$^{1\text{-}145}$ and ZmGDIα$^{146\text{-}291}$. The LUC activity was observed when ZmGA2ox7.3 was co-expressed with ZmGDIα$^{146\text{-}291}$, but not with ZmGDIα$^{1\text{-}145}$ (Supplementary Fig. 5c). Consistent with our previous study[5], the same four segments (ZmGDIα$^{334\text{-}390}$, ZmGDIα$^{334\text{-}378}$, ZmGDIα$^{379\text{-}445}$, and ZmGDIα$^{391\text{-}445}$) were co-expressed with ZmGA2ox7.3. Except for ZmGDIα$^{334\text{-}378}$, all the segments exhibited LUC activity, indicating that the C-terminal ZmGDIα$^{379\text{-}445}$ region can bind to ZmGA2ox7.3 (Supplementary Fig. 5c). Moreover, when the four fragments containing the ZmGDIα$^{334\text{-}378}$ segment (ZmGDIα$^{292\text{-}390}$, ZmGDIα$^{292\text{-}378}$, ZmGDIα-hel$^{292\text{-}375}$, and ZmGDIα-hel$^{292\text{-}363}$) were individually co-expressed with ZmGA2ox7.3, LUC activity was observed in all cases (Supplementary Fig. 5d). This indicates that ZmGDIα$^{334\text{-}378}$ does not hinder its flanking regions from interacting with ZmGA2ox7.3.

To validate these interactions, we selected four segments, ZmGDIα$^{1\text{-}145}$, ZmGDIα$^{146\text{-}333}$, ZmGDIα-hel$^{146\text{-}318}$, and ZmGDIα$^{379\text{-}445}$, to test their interactions with ZmGA2ox7.3. In the pull-down assay, ZmGA2ox7.3 interacted strongly with ZmGDIα$^{146\text{-}333}$ and ZmGDIα$^{379\text{-}445}$, but not with ZmGDIα$^{1\text{-}145}$ or ZmGDIα-hel$^{146\text{-}318}$ (Supplementary Fig. 5e). Similarly, in the BiFC assay, ZmGA2ox7.3 interacted strongly with ZmGDIα$^{146\text{-}333}$ and ZmGDIα$^{379\text{-}445}$, weakly with ZmGDIα-hel$^{146\text{-}318}$, but not at all with ZmGDIα$^{1\text{-}145}$ (Supplementary Fig. 5f). Hence, segments ZmGDIα$^{146\text{-}333}$ and ZmGDIα$^{379\text{-}445}$ play pivotal roles in the interaction with ZmGA2ox7.3, while the *helitron*-derived exon 10 in ZmGDIα-hel diminishes this interaction. Taken together, we hypothesize that P7-1, ZmGDIα (or ZmGDIα-hel), and ZmGA2ox7.3 can interact with one another, with P7-1/ZmGDIα/ZmGA2ox7.3 forming a tighter complex compared to P7-1/ZmGDIα-hel/ZmGA2ox7.3.

The ZmGDIα/P7-1 complex promotes the expression of *ZmGA2ox7.3*

Given the dramatic increase in *ZmGA2ox7.3* expression in NIL-S 16 days after viral infection (Fig. 1e), we sought to determine whether viral effectors, ZmGDIα, or both manipulate the expression of *ZmGA2ox7.3*, and what the difference is between the two ZmGDIα isoforms. Thus, we performed dual-luciferase transient expression assays using protoplasts of the two NILs. The reporter with the 3.0-kb *ZmGA2ox7.3* promoter was co-transformed with the effector constructs overexpressing viral cDNAs (Supplementary Fig. 6a). Out of the 13 effectors, P7-1 exhibited significantly higher normalized LUC activity in the NIL-S protoplasts compared to the empty vector control, followed closely by P6. No significant differences were found for the remaining effectors (Supplementary Fig. 6b). In contrast, in NIL-R protoplasts, the LUC activities either significantly decreased (for P5-2, P6, P7-*2*, and P10) or remained unchanged (for P1-P5-1, P7-1, P8, P9-1 and P9-2) compared to empty vector controls (Supplementary Fig. 6c). Similarly, in susceptible B73 protoplasts, P7-1 showed significantly higher LUC activity compared to the empty vector control (Supplementary Fig. 6d).

Next, we transiently expressed the *35S:GFP* or *35S:S7-1-GFP* constructs in protoplasts isolated from the two NILs. In NIL-S protoplasts, the expression of *ZmGA2ox7.3* was induced by ~2-fold when transformed with P7-1-GFP compared to GFP. However, in NIL-R protoplasts, the expression of *ZmGA2ox7.3* showed no difference between P7-1-GFP and GFP (Supplementary Fig. 6e). Furthermore, the expression of *ZmGA2ox7.3* was also significantly elevated in four transgenic lines overexpressing *S7-1-GFP* (Supplementary Fig. 6f–h). Collectively, the viral P7-1 effector, when paired with ZmGDIα, can significantly enhance the gene expression of *ZmGA2ox7.3*. However, this effect was not observed with ZmGDIα-hel.

ZmGA2ox7.3 can form oligomers in the presence of GA_4

The rice OsGA2ox3 can oligomerize when exposed to GA_4[27]. Being the close homolog in maize, ZmGA2ox7.3 might also undergo oligomerization in the presence of GA_4. In the SLC assay, we observed that ZmGA2ox7.3 can interact with itself (Fig. 5a), a finding later confirmed by in vivo Co-IP and in vitro pull-down assays (Fig. 5b, c). Furthermore, both SLC and BiFC assays affirmed that exogenous GA_4 treatment can significantly enhance the ZmGA2ox7.3 self-association (Fig. 5d, e). In rice, the oligomerization of OsGA2ox3 was reported to depend on three essential amino acids: C194, K308, and K313[27]. Sequence alignment revealed that ZmGA2ox7.3 shares the first two amino acids at positions 198 and 312, respectively, and the third residue at the

https://doi.org/10.1038/s41467-024-51726-7

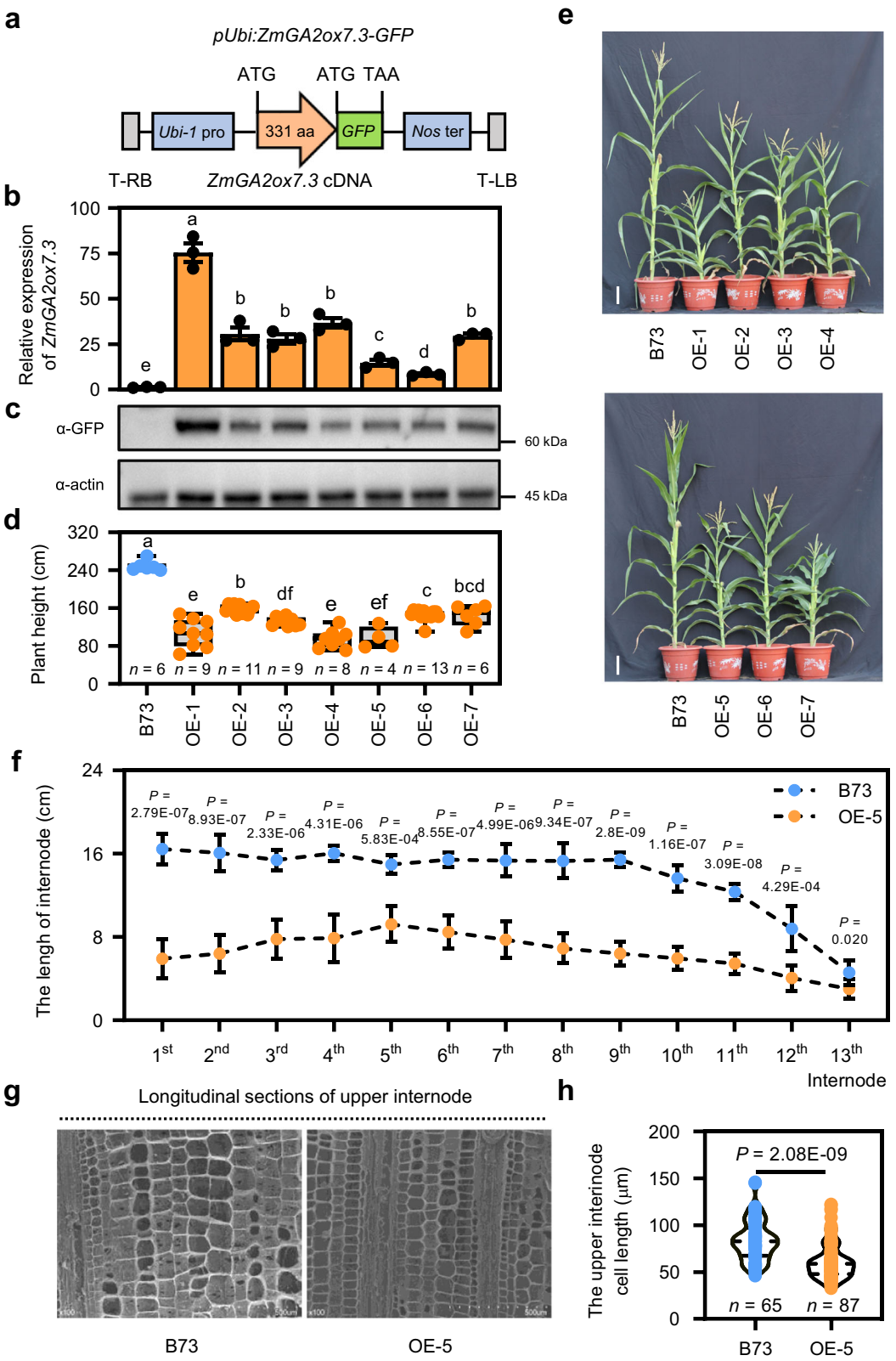

position 317 is Arg (R) (Supplementary Fig. 3b). We mutated C198, K312, and R317 to Ala (A) simultaneously to generate the ZmGA2ox7.3^{3A} variant. In the SLC assay, the ZmGA2ox7.3^{3A} variant failed to undergo self-association, even when treated with exogenous GA_4 (Fig. 5f). To assess molecular weights for potential oligomers of ZmGA2ox7.3 in gel filtration chromatography, we established a standard curve by plotting the peak volume against the corresponding molecular weight (Fig. 6a, b). We immunopurified both GST-ZmGA2ox7.3 and GST-ZmGA2ox7.3^{3A} (Fig. 6c). When exposed to 0.5 mM GA_4, multiple peaks were observed for ZmGA2ox7.3 in the gel filtration profile; however, these were significantly diminished in the absence of GA_4. In contrast, ZmGA2ox7.3^{3A} exhibited no evident peaks, irrespective of the presence or absence of GA_4. Based on the standard curve, these peaks corresponded to the ZmGA2ox7.3 tetramer (designated as 'T',

https://doi.org/10.1038/s41467-024-51726-7

Fig. 2 | Overexpression of *ZmGA2ox7.3* causes dwarf plants. a Schematic diagram of the overexpression construct *pUbi:ZmGA2ox7.3-GFP*. **b**, **c** Confirmation of seven transgenic events overexpressing *ZmGA2ox7.3* ($n = 3$). The relative expression levels of *ZmGA2ox7.3* in the transgenic lines (**b**). Immunoblot analysis of the exogenous ZmGA2ox7.3-GFP using an anti-GFP antibody, and of the actin protein using an anti-actin antibody (**c**). The B73 recipient line served as a negative control. A biological replicate in the B73 serve as a control sample for relative expression (**b**). **d**, **e** Plant heights of the transgenic lines overexpressing *ZmGA2ox7.3*. Statistical analysis of plant heights comparing B73 with the transgenic lines (**d**). The plant morphology of both B73 and the transgenic lines (**e**). Scale bar, 30 cm. **f** Measurement of internode lengths of B73 ($n = 6$) and *ZmGA2ox7.3* overexpression line OE-5 plants ($n = 7$), starting from the uppermost internode (the first stem node) and progressing downwards. **g**, **h** Characteristics of cells in the uppermost internode. Images of transections comparing B73 with OE-5 (**g**). Statistical analysis of cell lengths between B73 and OE-5 (**h**). Scale bar, 500 μm (white dashed line). In (**b**, **f**), data represent the mean ± s.e.m, individual data points are depicted. In (**d**), box plots are displayed. Error bars represent the maximum and minimum values; the central lines show the medians; and the box edges denote the 25th and 75th percentiles. In (**h**), data are shown as violin plots with individual data points. Statistical differences ($P < 0.05$) are highlighted using different lowercase letters, as determined by Kruskal-Wallis test (**b**, **d**). Significance levels are determined by a two-tailed Student's *t*-test (**f**) and two-sided Mann–Whitney U test (**f**, **h**).

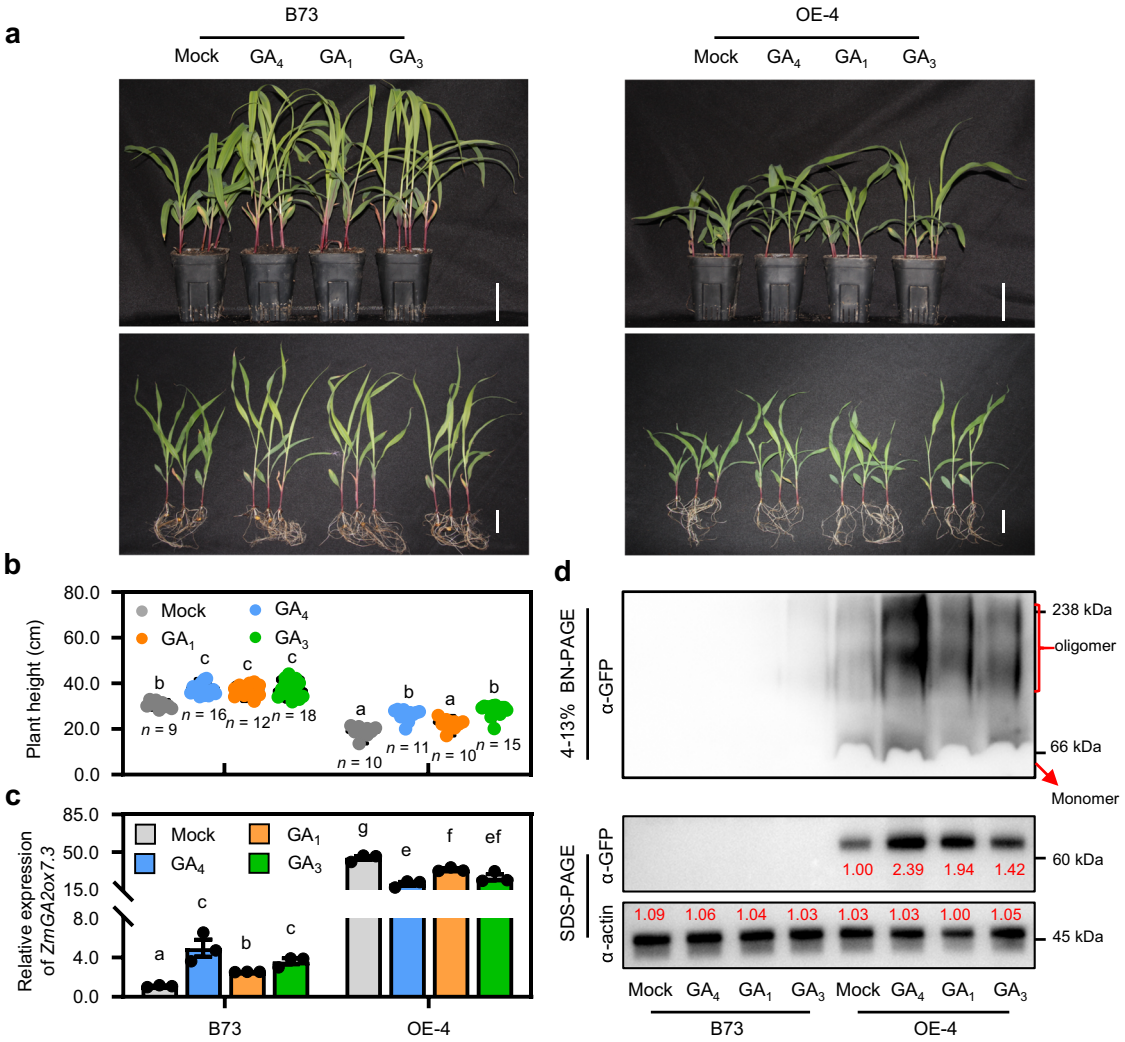

Fig. 3 | The phenotype of overexpression of *ZmGA2ox7.3* to treatments with exogenous GAs. a, **b** Responses of B73 and OE-4 to treatments with GA_1, GA_3 or GA_4. The plant morphology before and after GA_1, GA_3 or GA_4 treatment (**a**). Statistical analysis of plant heights between B73 and OE-4 (**b**). Mock, 0.1% Tween 20 served as a negative control. Scale bar, 10 cm. **c** The relative expression levels of *ZmGA2ox7.3* in B73 and OE-4 before and after treatments with GA_1, GA_3 and GA_4, respectively ($n = 3$). A biological replicate in the B73 mock serve as a control sample for relative expression. **d** The exogenous ZmGA2ox7.3-GFP proteins of OE-4 treated with GA_4, GA_1 or GA_3 were subjected to 4–13% BN-PAGE and SDS-PAGE, followed by immunoblotting with an anti-GFP antibody, and of the actin protein immunoblotting with an anti-actin antibody, respectively. The B73 recipient line served as a negative control. In (**b**), data are shown as violin plots with individual data points. In (**c**), data represent the mean ± s.e.m, individual data points are depicted. Statistical differences ($P < 0.05$) are highlighted using different lowercase letters, as determined by Kruskal–Wallis test (**b**, **c**).

~240 kDa), dimer (designated as 'D', ~120 kDa), and monomer (designated as 'M', ~60 kDa), respectively (Fig. 6d). We also collected elution fractions of the three peaks of GA_4-treated ZmGA2ox7.3 and displayed their compositions using blue native polyacrylamide gel electrophoresis (BN-PAGE) (Fig. 6e). Next, we compared the 'T' peaks (11.0–11.5 ml) between ZmGA2ox7.3 and its variant ZmGA2ox7.3^{3A}. In the presence of GA_4, a prominent band of ZmGA2ox7.3 tetramer emerged, while it was fainter without GA_4. For ZmGA2ox7.3^{3A}, there was hardly any discernible bands. The intensities of these bands were further confirmed on an SDS-PAGE gel (Fig. 6f). These findings highlight the importance of GA_4 and the three key residues (K198, K312, and R317) in the GA-dependent oligomerization of ZmGA2ox7.3.

https://doi.org/10.1038/s41467-024-51726-7

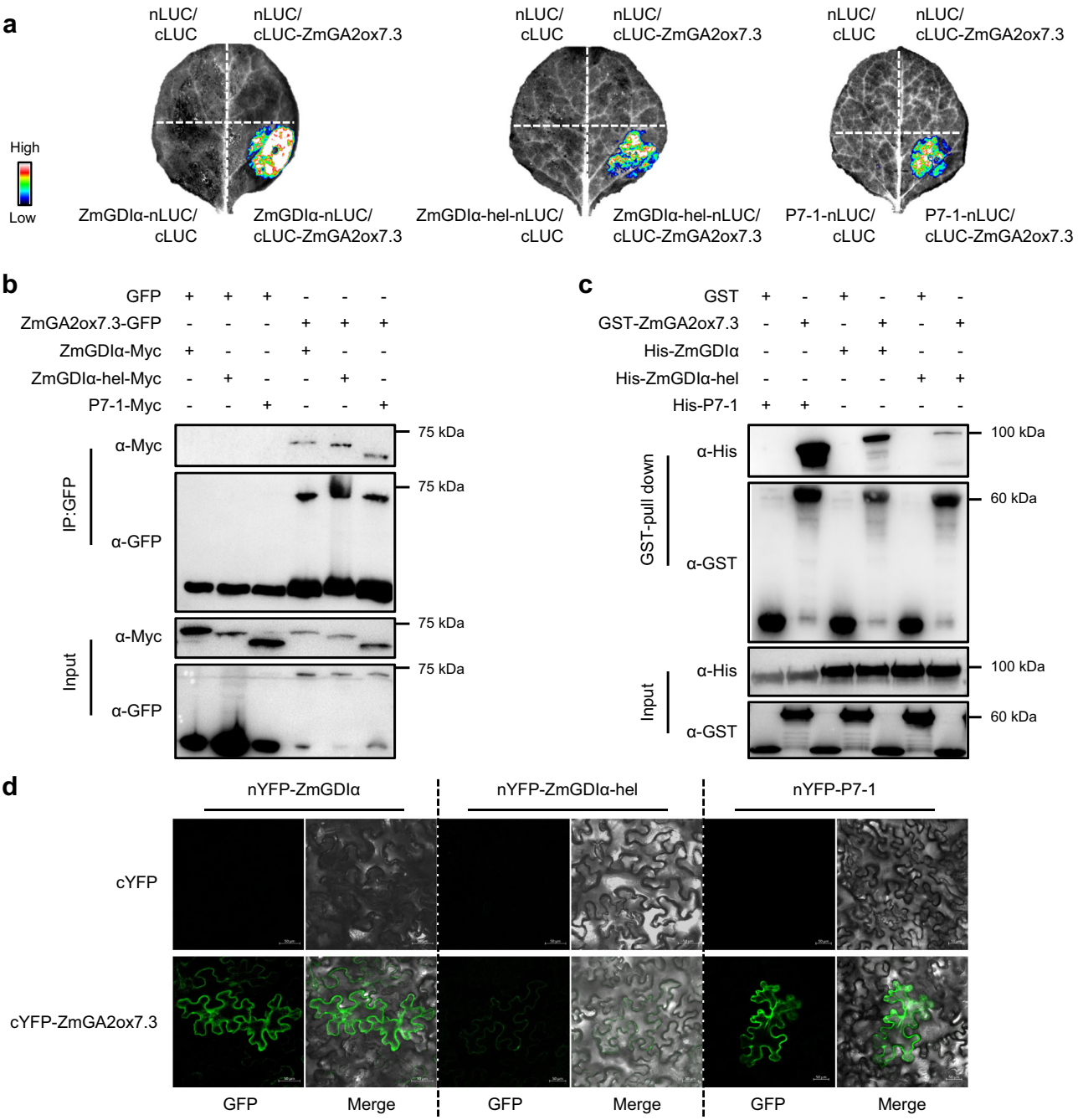

Fig. 4 | The interactions of ZmGA2ox7.3 with ZmGDIα, ZmGDIα-hel, and P7-1. **a** Validation of the interactions of ZmGA2ox7.3 with ZmGDIα, ZmGDIα-hel, or P7-1 using an in vivo SLC assay. The color scale depicts the intensity of the luminescence signals. **b** Confirmation of the interactions of ZmGA2ox7.3 with ZmGDIα, ZmGDIα-hel or P7-1 using a Co-IP assay. **c** Confirmation of the interactions of ZmGA2ox7.3 with ZmGDIα, ZmGDIα-hel, or P7-1 using an in vitro GST-pull down assay. **d** Confirmation of the interactions of ZmGA2ox7.3 with ZmGDIα, ZmGDIα-hel, or P7-1 using an in vivo BiFC assay. Reconstituted YFP fluorescence signals were visualized using confocal microscopy and captured at 72 h post inoculation (hpi). Scale bar, 50 μm. The Co-IP, pull-down and BiFC assays were repeated at least four times.

Enzymatic activity of ZmGA2ox7.3 is mainly due to its oligomerization

In rice, the formation of OsGA2ox3 multimers is known to determine its enzymatic activity[27]. Inspired by this, we posed two questions: (1) Does the formation of ZmGA2ox7.3 oligomers, similar to its rice counterpart, influence its enzymatic activity? (2) Do the ZmGA2ox7.3-interacting proteins, specifically P7-1 and the two ZmGDIα isoforms, affect its enzymatic activity as well?

We firstly overexpressed *ZmGA2ox7.3* and *ZmGA2ox7.3*^{3A} in *Arabidopsis*, with each construct yielding two independent transgenic events. As anticipated, overexpression of *ZmGA2ox7.3* induced a dwarf phenotype, while overexpression of *ZmGA2ox7.3*^{3A} did not lead to dwarfing (Fig. 6g). Considering that ZmGA2ox7.3^{3A} was unable to form oligomers, this observation implies that the formation of the ZmGA2ox7.3 oligomer is a prerequisite for its enzymatic activity.

To assess the enzymatic activity of ZmGA2ox7.3, we developed an assay by detecting the product GA_{34} while using GA_4 as the substrate, modified from previous studies (Supplementary Fig. 3c)[25,26]. We prepared five distinct concentrations of GA_4 and mixed each with 1 mg of ZmGA2ox7.3 (Fig. 7a). The enzymatic activity of ZmGA2ox7.3 was

https://doi.org/10.1038/s41467-024-51726-7

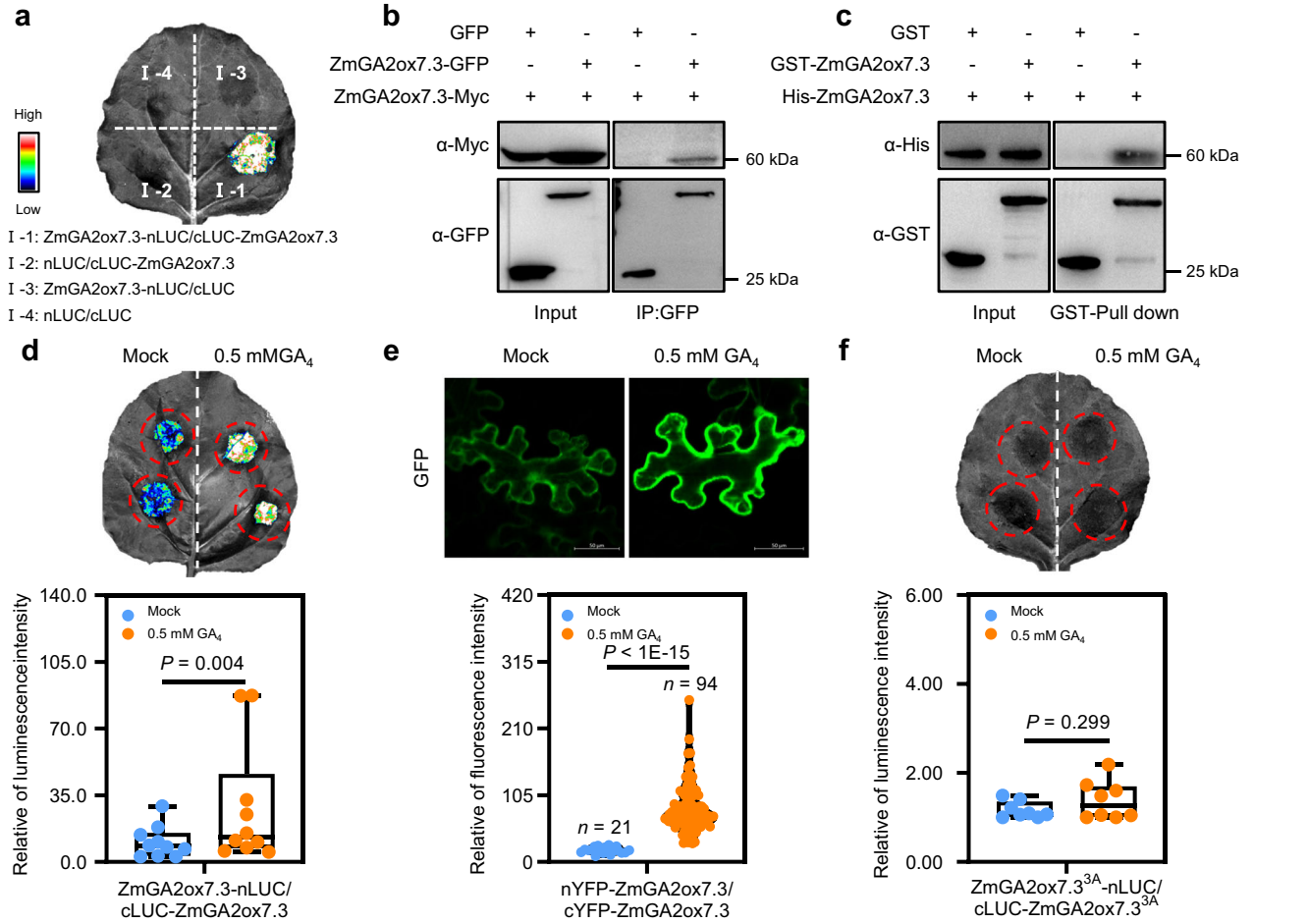

Fig. 5 | The bioactive GA_4 promotes oligomerization of ZmGA2ox7.3 but not its variant ZmGA2ox7.3^{3A}. **a** The self-association of ZmGA2ox7.3 in an SLC assay. The color scale denotes the intensity of the luminescence signal. **b** Confirmation of the self-interaction of ZmGA2ox7.3 using a Co-IP assay. **c** Confirmation of the self-interaction of ZmGA2ox7.3 using an in vitro pull-down assay. **d** The impact of GA_4 on ZmGA2ox7.3 self-association in the SLC assay ($n = 10$). **e** The impact of GA_4 on ZmGA2ox7.3 self-interaction in the BiFC assay. **f** The self-interaction of the variant ZmGA2ox7.3^{3A} with or without GA_4 in SLC assays ($n = 8$). In (**d**, **f**), data are presented as box plots, with error bars indicating the maximum and minimum values. The medians are indicated by the central lines, and the box edges represent the 25th and 75th percentiles. In (**e**), data are depicted as violin plots with individual data points. Significance levels are determined using two-sided Wilcoxon matched-pairs signed rank test (**d**), two-sided Mann–Whitney U test (**e**) or a two-tailed Student's *t* test (**f**). The Co-IP and pull-down assays were repeated at least three times.

detectable at GA_4 concentrations as low as 5×10^{-4} mM, and augmented with increasing GA_4 concentration. This activity plateaued at 0.5 mM GA_4 and did not increase further, even with GA_4 concentrations up to 5 mM (Fig. 7b). In parallel, we observed a proportional increase in the content of ZmGA2ox7.3 tetramers and dimers as the GA_4 concentration increased, culminating at 0.5 mM GA_4 on the gel filtration profile. Intriguingly, the curves for 0.5 mM and 5 mM GA_4 coincided perfectly, despite a tenfold disparity in GA_4 concentration (Fig. 7c). A strong relationship was observed between the content of ZmGA2ox7.3 oligomers (tetramers and dimers) and the GA_{34} product, with a correlation coefficient of 0.9819 (Fig. 7d). Moreover, we collected elution fractions from the 'T' and "D" peaks and subjected them to immunoblotting with an anti-GST antibody on BN-PAGE. The intensity of the ZmGA2ox7.3 oligomeric bands aligned well with its enzymatic activity across different GA_4 concentrations (Fig. 7e). These results indicate that the quantity of ZmGA2ox7.3 oligomers directly reflect its enzymatic activity.

The ZmGDIα/P7-1 complex affects the enzymatic activity of ZmGA2ox7.3

To elucidate how the interaction of ZmGA2ox7.3 with P7-1, ZmGDIα or ZmGDIα-hel affects its enzymatic activity, we immunopurified all four proteins: MBP-P7-1, His-ZmGDIα, His-ZmGDIα-hel, and GST-ZmGA2ox7.3. Equal amounts of GST-ZmGA2ox7.3 were mixed with one or two of the other three proteins to prepare six distinct combinations (I: GST-ZmGA2ox7.3 + MBP + GST; II: GST-ZmGA 2ox7.3 + MBP-P7-1 + GST; III: GST-ZmGA2ox7.3 + MBP+His-ZmGDIα; IV: GST-ZmGA2ox7.3 + MBP-P7-1+His-ZmGDIα; V: GST-ZmGA2ox7.3 + MBP+His-ZmGDIα-hel; VI: GST-ZmGA2ox7.3 + MBP-P7-1+His-ZmGDIα-hel) (Fig. 8a). When exposed to 0.5 mM GA_4, all six combinations displayed multiple oligomers in the gel filtration profile. In addition to the previously identified 'T', 'D', and 'M' peaks, we detected new 'Mu' peaks in combinations III (ZmGA2ox7.3/ZmGDIα) and IV (ZmGA2ox7.3/ZmGDIα/P7-1). However, these 'Mu' peaks nearly vanished when ZmGDIα was substituted by ZmGDIα-hel (Fig. 8b). We collected elution fractions from the two 'Mu' peaks and analyzed their molecular weights using BN-PAGE and compositions via mass spectrometry. The 'Mu' peak for combination III included a ZmGA2ox7.3 oligomer with ZmGDIα (~10.21 ml, ~410 kDa), while that for combination IV had a ZmGA2ox7.3 oligomer with ZmGDIα/P7-1 (~10.19 ml, ~440 kDa) (Fig. 8b–d). We also conducted immunoblotting assays to analyze the compositions of eluted fractions collected from the 'Mu' (10.0 to 10.5 ml) and 'T' (11.0 to 11.5 ml) peaks across all six combinations. In the 'Mu' fractions, the content of ZmGA2ox7.3 was significantly higher in the combination IV than in other combinations (Fig. 8e). Conversely, in the 'T' fractions, the content of ZmGA2ox7.3 was

https://doi.org/10.1038/s41467-024-51726-7

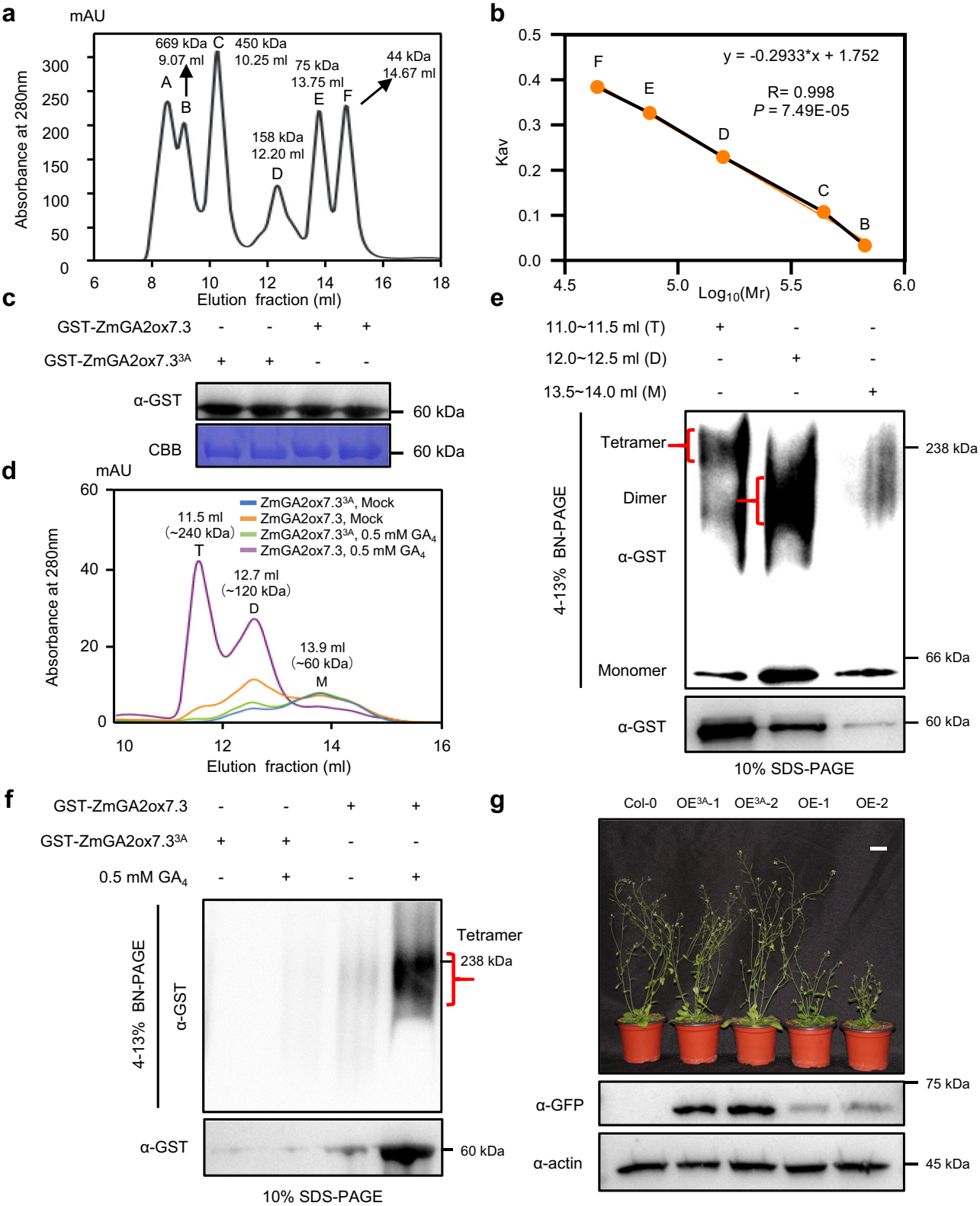

Fig. 6 | The formation of oligomer ZmGA2ox7.3 depends on bioactive GA_4. **a** Chromatographic separation of a mixture of five standard proteins. **b** Plots of calibration curves for standard proteins. "R" indicates the correlation efficiency. **c** The quantities of purified GST-ZmGA2ox7.3 and GST-ZmGA2ox7.3^{3A}. **d** The gel filtration profiles of ZmGA2ox7.3 and ZmGA2ox7.3^{3A} with or without 0.5 mM GA_4. The peaks correspond to the tetramer (T), dimer (D), and monomer (M) forms. **e** The molecular weights of the "T", "D", and "M" peaks of ZmGA2ox7.3 in the presence of 0.5 mM GA_4. **f** The eluted "T" peak fractions from ZmGA2ox7.3 and ZmGA2ox7.3^{3A} with or without 0.5 mM GA_4. **g** The plant morphology of Col-0, OE-ZmGA2ox7.3^{3A}, and OE-ZmGA2ox7.3 in *Arabidopsis thaliana*. The exogenous ZmGA2ox7.3-GFP^{3A} and ZmGA2ox7.3-GFP proteins were detected using immunoblotting with anti-GFP antibodies. Scar bar, 5 cm. Significance level was determined by a two-sided simple linear regression statistical test (**b**). The gel filtration chromatography assays were repeated three times.

https://doi.org/10.1038/s41467-024-51726-7

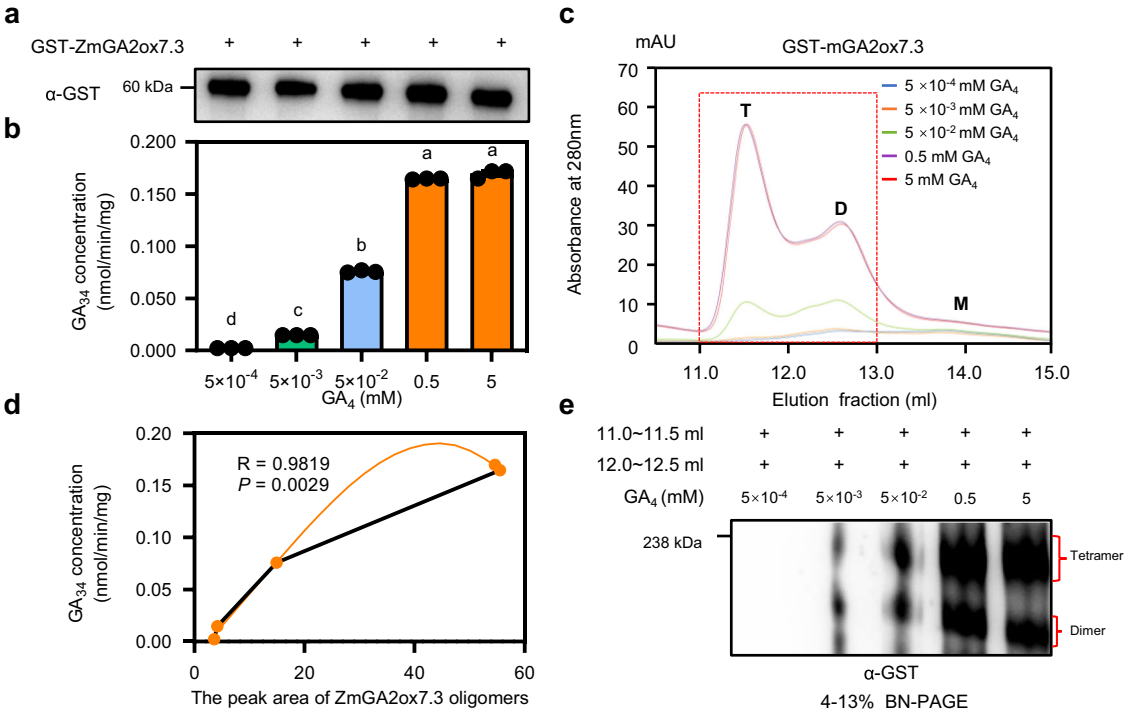

Fig. 7 | Oligomerization of ZmGA2ox7.3 is closely associated with its enzymatic activity. a Detection of the purified GST-ZmGA2ox7.3. **b** The enzymatic activity of ZmGA2ox7.3 across a range of GA_4 concentrations, as measured by quantifying the product GA_{34} ($n = 3$). **c** The gel filtration curves of ZmGA2ox7.3 under various concentrations of GA_4. The peaks observed, from left to right, correspond to tetramer (T), dimer (D), and monomer (M). **d** The correlation between the product GA_{34} and the peak area of ZmGA2ox7.3 oligomers (the red dashed box section in **c**) at various concentrations of GA_4. "R" indicates the Pearson's correlation efficiency. **e** Quantitation of ZmGA2ox7.3 tetramers and dimers (oligomers) under various concentrations of GA_4. The eluted peak fractions (11.0–11.5 ml) and (12.0–12.5 ml) were subjected to 4–13% BN-PAGE, followed by immunoblotting with an anti-GST antibody. In (**b**), data (mean ± s.d.) are presented with individual data points, where different lowercase letters indicate a significant difference ($P < 0.05$) based on one-way ANOVA with Tukey's test and two-sided Pearson R statistical test (**d**). The gel filtration chromatography assay was repeated three times.

significantly higher in the combination I than in other combinations (Fig. 8f). When considering both the 'Mu' and 'T' fractions together, ZmGDIα did not significantly influence the oligomerization of ZmGA2ox7.3, whereas ZmGDIα-hel severely hindered this oligomerization. Notably, MBP-P7-1 could further enhance the formation of the ZmGA2ox7.3 oligomer when combined with ZmGDIα, but not with ZmGDIα-hel (Fig. 8e, f).

With the same six combinations, we examined the potential impacts of P7-1 and the two ZmGDIα isoforms on the enzymatic activity of ZmGA2ox7.3. Compared to the mixture of 0.5 mM GA_4 and GST-ZmGA2ox7.3 (combination I), the addition of MBP-P7-1 (combination II) led to a significant reduction in the GA_{34} product. In contrast, adding His-ZmGDIα (combination III) did not significantly affect the GA_{34} product. When both MBP-P7-1 and His-ZmGDIα were added simultaneously (combination IV), a significant increase in the GA_{34} product was observed. However, the inclusion of His-ZmGDIα-hel led to a significant decrease in the GA_{34} product, regardless of the absence (combination V) or presence (combination VI) of MBP-P7-1 (Fig. 8g). Taken together, these results suggest that the oligomerization and enzymatic activity of ZmGA2ox7.3 can be enhanced when mixed with ZmGDIα/P7-1, but are considerably diminished when ZmGDIα-hel replaces ZmGDIα.

Viral infection impairs the subcellular structures of susceptible maize

To decipher the cytological changes caused by RBSDV infection that leads to MRDD symptoms, we observed the internode cells in the diseased NIL-S and the heathy NIL-R. The diseased NIL-S plants exhibited typical symptoms of stunted growth and shortened internodes compared to the healthy NIL-R plants (Supplementary Fig. 7a, b, g, h). In the upper internodes of the diseased NIL-S plants, devastating changes in subcellular structures were observed, including significant thickening of the cell walls and rupture of both the cell and organelle membranes (Supplementary Fig. 7c–f). In contrast, the cytoplasm in the healthy NIL-R plants was tightly organized around the cell membrane (Supplementary Fig. 7i–l). Notably, numerous virions were detected in the cytoplasm of the diseased NIL-S plants, while no viral particles were found in the healthy NIL-R plants (Supplementary Fig. 7e, f, k, l).

RBSDV-induced phytohormone change underlies MRDD symptoms

To explore the mechanism by which RBSDV infection leads to MRDD symptoms, we used the two NILs to measure the levels of various GAs during viral infection. We infested maize seedlings at the budding stage with viruliferous planthoppers and harvested upper internodes (the shortest upper stem nodes) and upper leaves (the areas around white waxy enations) at 60 dpi. We then assessed the relative expression of the viral *S7-1* and quantified the levels of eight GAs (GA_1, GA_4, GA_8, GA_9, GA_{20}, GA_{34}, and GA_{51}). In the upper internodes, the *S7-1* mRNA accumulated significantly more in NIL-S than in NIL-R after RBSDV infection (Fig. 9a). Comparatively, following viral infection, NIL-S exhibited a pronounced decrease in the levels of bioactive GA_4, its product GA_{34} and precursor GA_9, relative to NIL-R (Fig. 9b). Additionally, RBSDV-infected NIL-S displayed substantially reduced levels of bioactive GA_1 and its product GA_8. Intriguingly, RBSDV infection led to a remarkable increase in GA_{29} levels in both NIL-S and NIL-R (Fig. 9b). These findings provide insights into the severe internode

https://doi.org/10.1038/s41467-024-51726-7

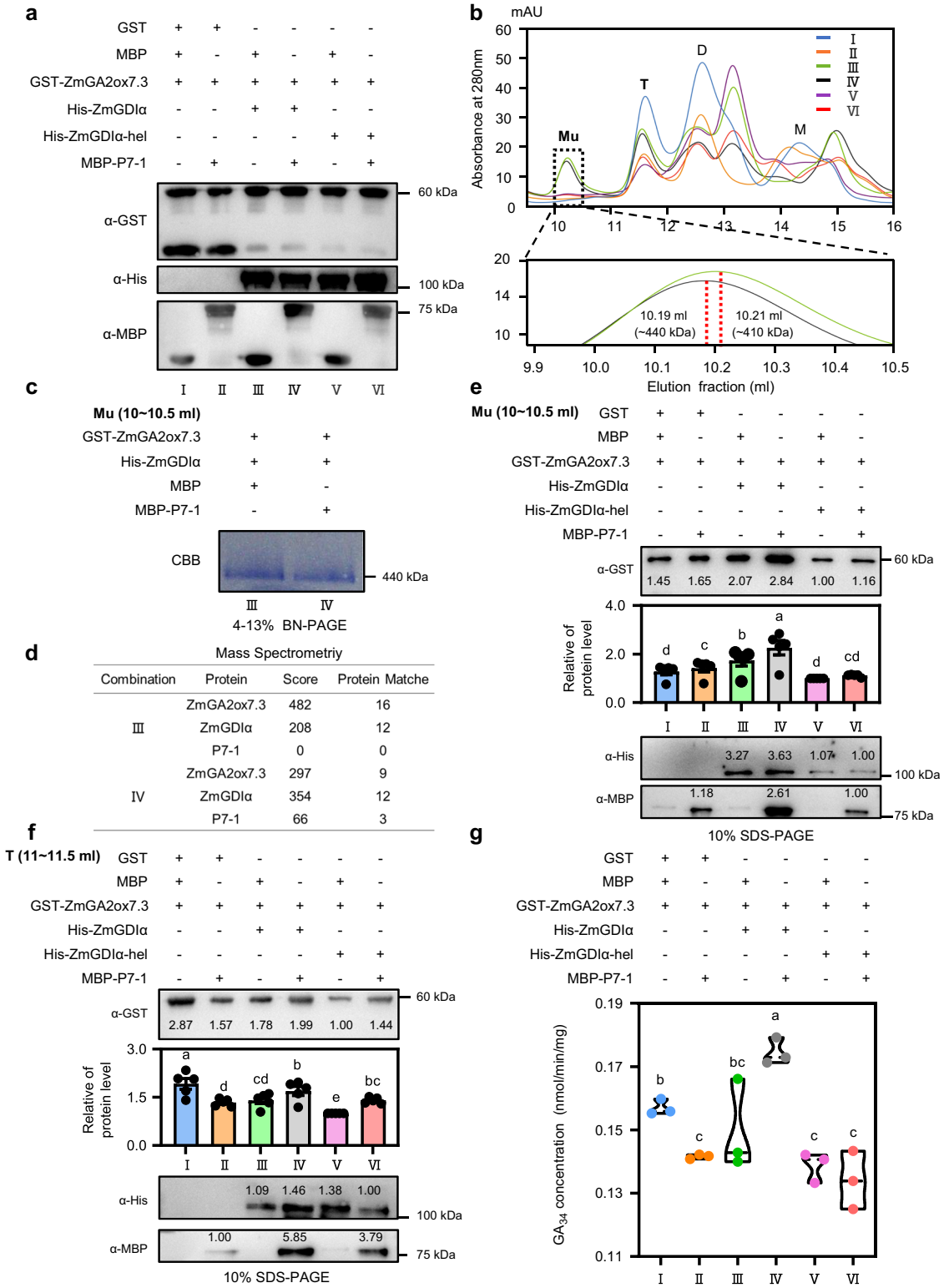

Fig. 8 | The ZmGDIα/P7-1 complex enhances the enzymatic activity of ZmGA2ox7.3. a The compositions of six combinations. The mixtures were verified on a 10% SDS-PAGE gel using an immunoblotting assay. **b** The gel filtration curves of oligomerized proteins from six combinations in the presence of GA_4. The peaks correspond to multimer (Mu), tetramer (T), dimer (D), and monomer (M). The "Mu" peak was enlarged and placed below. **c**, **d** Analysis of compositions of the "Mu" peaks appeared in combinations III and IV. The eluted "Mu" peak fractions were stained with Coomassie brilliant blue (**c**). The various proteins were revealed by the LC-MS assay (**d**). **e**, **f** Quantification of ZmGA2ox7.3 oligomers for the "Mu" and "T" peaks from six combinations ($n = 5$). The eluted "Mu" (10.0–10.5 ml) (**e**) and "T" (11.0–11.5 ml) (**f**) fractions were subjected to 10% SDS-PAGE, followed by immunoblotting using anti-GST (for GST-ZmGA2ox7.3), anti-His (for His-ZmGDIα/His-ZmGDIα-hel), and anti-MBP (for MBP-P7-1) antibodies. **g** Measurement of enzymatic activities of ZmGA2ox7.3 for six combinations in the presence of 0.5 mM GA_4. In (**e**, **f**), data (mean ± s.d.) are presented with individual data points, data are depicted as violin plots with individual data points (**g**). Different lowercase letters indicate a significant difference ($P < 0.05$) based on Kruskal–Wallis test (**e**) or one-way ANOVA with Tukey's test (**f**, **g**). The gel filtration chromatography assay was repeated at least five times.

https://doi.org/10.1038/s41467-024-51726-7

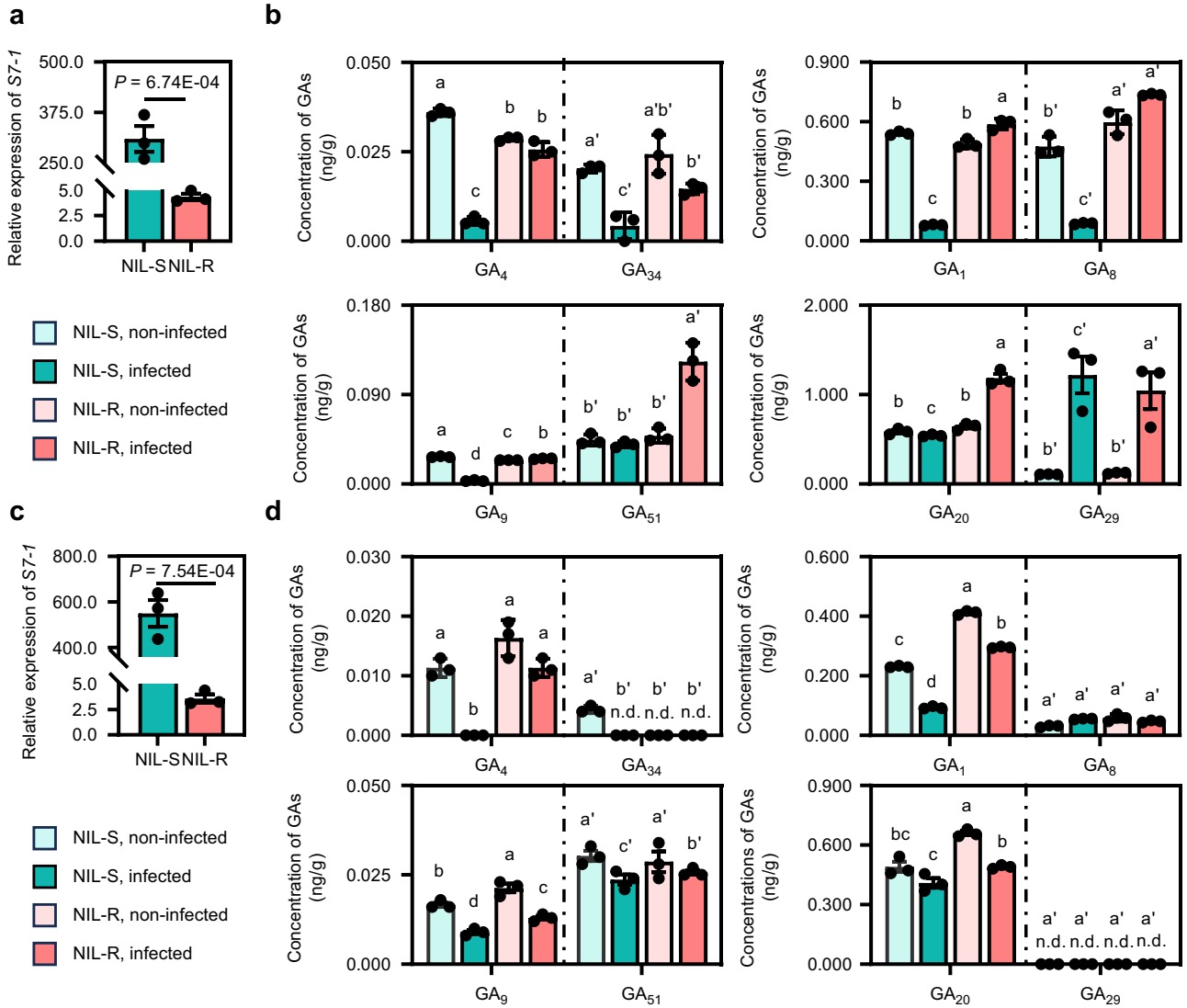

Fig. 9 | RBSDV infection severely reduces the active gibberellins in the upper internodes and upper leaves of the two NILs, and a working model for the development of MRDD symptoms. The relative expression of RBSDV *S7-1* in the upper internodes (**a**) and upper leaves (**c**) of the two NILs at 60 dpi ($n = 3$). The contents of eight gibberellins in the upper internodes (**b**) and upper leaves (**d**) of the two NILs at 60 days after infestation with either RBSDV-carrying or RBSDV-free planthoppers ($n = 3$). In (**a**, **c**), data (mean ± s.e.m.) are presented with individual data points, as determined by a two-tailed Student's *t* test. In (**b**, **d**), data represent the mean ± s.d. and different lowercase letters indicate a significant difference ($P < 0.05$) based on one-way ANOVA with Tukey's test.

shortening observed in RBSDV-infected NIL-S, as opposed to the unaffected NIL-R.

In the upper leaves as well, the *S7-1* mRNA accumulated significantly more in NIL-S than in NIL-R (Fig. 9c). In the infected NIL-S, the level of bioactive GA_4 nearly vanished, and there was also a significant decrease in the level of another bioactive GA_1. Additionally, other GAs, such as GA_9 and GA_{51} were also reduced, and GA_{29} and GA_{34}, were barely detectable (Fig. 9d). In NIL-R, there was no significant difference in the active GA_4 levels pre- and post-viral infection. However, the other active GA_1, along with four additional GAs (GA_1, GA_8, GA_9, and GA_{20}), exhibited a significant reduction, though not as pronounced as in NIL-S. Both GA_{29} and GA_{34} were not detected (Fig. 9d).

The white waxy enations on the abaxial side of the upper leaf veins arise from the abnormal proliferation of phloem cells in the vascular bundle[5]. Given the involvement of auxin, cytokinins, and GAs in cell expansion, we sought to ascertain whether auxin and cytokinins also contribute to the formation of white waxy enations. To do this, the two NILs were infested with viruliferous and non-viruliferous planthoppers, respectively. We collected samples at 16 and 60 dpi to assess auxin levels at both time points and cytokinin levels at 60 dpi, respectively. Following viral infection, RBSDV accumulated significantly in NIL-S but only slightly in NIL-R, as evidenced by the relative expression of viral *S10* and *S7-1* at 16 dpi (Supplementary Fig. 8a, b). Concurrently, the auxin content in the upper leaves significantly increased in NIL-S, but remained unchanged in NIL-R. Under non-infected conditions, no difference in auxin levels was observed between NIL-S and NIL-R (Supplementary Fig. 8c).

By 60 dpi, both NILs displayed significantly elevated auxin levels in both the upper leaves and internodes compared to the uninfected control, with the auxin content in NIL-R surpassing that in NIL-S, particularly in the upper internodes (Supplementary Fig. 8d, e). Finally, we evaluated the cytokinin levels in the upper leaves. During the late stage of RBSDV infection, the concentrations of six cytokinins (iP, iPR, tZ, tZR, cZ and HZD) were significantly higher in NIL-R than in NIL-S, with two exceptions being cZR and DHZR (Supplementary Fig. 8f).

The observed fluctuations in the three growth-promoting phytohormones underscore the profound disturbance of phytohormone balance in NIL-S following RBSDV infection. The coordinated

https://doi.org/10.1038/s41467-024-51726-7

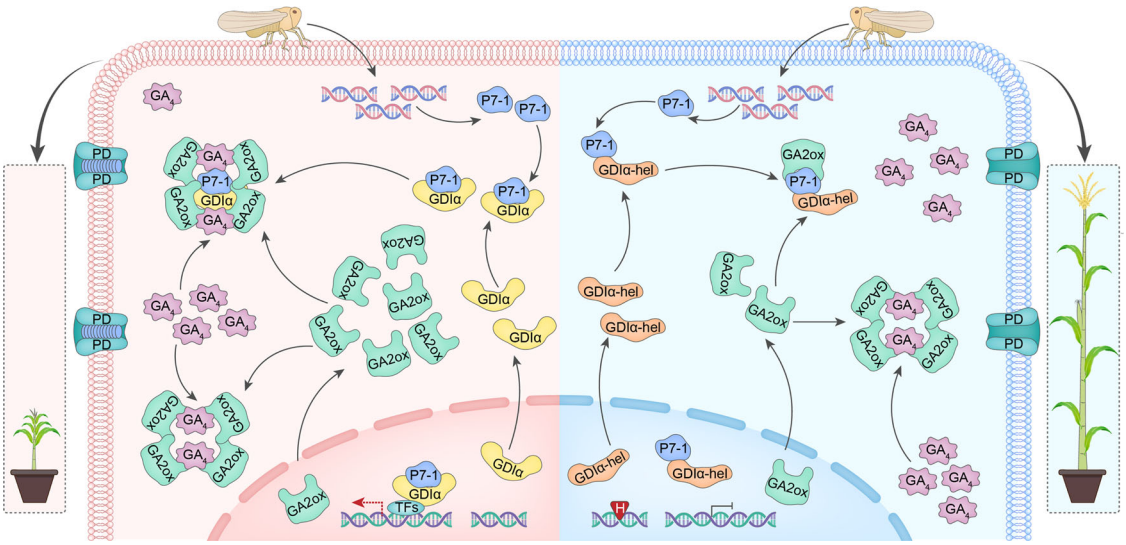

Fig. 10 | A working model for the development of MRDD symptoms. Left: RBSDV infection in NIL-S substantially stimulates the expression of *ZmGA2ox7.3* to form abundant ZmGA2ox7.3 oligomers. These can act either alone or combined with P7-1/ZmGDIα to reduce active GA_1/GA_4 levels, disrupt the balance of auxins and cytokinins, and ultimately induce MRDD symptoms. Right: RBSDV infection in NIL-R just slightly increases the expression levels of *ZmGA2ox7.3*, and the resultant low level of ZmGA2ox7.3 oligomers is insufficient to effectively reduce GA_1/GA_4 levels, eventually leading to MRDD resistance.

interactions among GAs, auxin, and cytokinins are crucial for the manifestation of MRDD syndrome, which is mainly characterized by dwarfism.

A working model for the development of MRDD symptoms

ZmGA2ox7.3 can form active oligomers to convert bioactive GA_1/GA_4 into inactive GA_8/GA_{34}. During RBSDV infection, the expression of *ZmGA2ox7.3* is substantially induced in NIL-S to produce abundant ZmGA2ox7.3 oligomers. These oligomers can act either independently or in conjunction with the P7-1/ZmGDIα complex to reduce GA_1/GA_4 levels, disrupt the balance of auxin and cytokinins, and ultimately induce MRDD symptoms. Conversely, the lower levels of ZmGA2ox7.3 oligomers in NIL-R are insufficient to effectively reduce GA_1/GA_4 levels, leading to MRDD resistance (Fig. 10).

Discussion

Viral proteins can hijack host target proteins to disrupt the balance of plant hormones, which are crucial for facilitating viral systemic infection, ultimately leading to the appearance of viral symptoms[24,30,31]. However, little is known about the molecular mechanisms underlying the manifestation of MRDD symptoms. Our previous study demonstrated that the viral P7-1 effector binds more tightly to ZmGDIα than to ZmGDIα-hel, which underpins the differential resistance to RBSDV. In this study, we discovered that P7-1 can recruit another host target, ZmGA2ox7.3, which also exhibits a tighter binding affinity to ZmGDIα than to ZmGDIα-hel. During RBSDV infection, the allelic variation at the *ZmGDIα* locus, caused by *helitron* insertion, greatly influences both the quantities and interactions among ZmGA2ox7.3, ZmGDIα/ZmGDIα-hel, and the viral P7-1. All these factors play crucial roles in reducing active gibberellins and, consequently, disrupting the balance of auxin and cytokinins in maize, thereby determining the outcome of MRDD. Our discovery thus elucidates the intricate molecular mechanisms that underlie the development of MRDD symptoms.

In susceptible maize, RBSDV infection could significantly enhance the gene expression of *ZmGA2ox7.3*. Given that no RBSDV protein serves as a transcription factor, the viral proteins likely recruit host transcription factors to promote *ZmGA2ox7.3* expression. Previous researches indicated that GA-2 oxidase family genes are regulated by multiple transcription factors[32,33]. Intriguingly, our previous Co-IP/MS assay revealed numerous transcription factors in immunoprecipitates associated with RBSDV infection, such as growth-regulating factor (GRF), AP2-EREBP, basic helix-loop-helix (bHLH), MADS-box, and GRAS (Supplemental Table 2). These findings suggest that, upon RBSDV invasion, the viral P7-1 effector may recruit certain maize transcription factors to promote the expression of *ZmGA2ox7.3*.

OsGA2ox3 forms GA_4-dependent multimers, displaying higher enzymatic activity than monomer[27]. Similarly, when exposed to GA_4, ZmGA2ox7.3 can form oligomers (tetramers and dimers) with enhanced catalytic activity, converting the bioactive GA_4 into its inactive GA_{34}. In the ZmGA2ox7.3^{3A} variant, the three mutated residues are solely associated with the formation of oligomers, but not with enzymatic activity[27]. The failure to form ZmGA2ox7.3^{3A} oligomers leads to the absence of enzymatic activity, indicating that oligomer formation is a prerequisite for the enzymatic activity. Given that ZmGA2ox7.3 tetramers and dimers exhibited simultaneous increases in the presence of GA_4, we thus cannot distinguish between them in their enzymatic activities. Therefore, we generally conclude that ZmGA2ox7.3 oligomers enhance enzymatic activity. In susceptible maize, RBSDV-triggered upregulation of ZmGA2ox7.3, combined with a massive accumulation of the viral P7-1 effector, leads to the formation of abundant ZmGA2ox7.3 oligomers. These oligomers, whether acting alone or in conjunction with ZmGDIα/P7-1, can efficiently convert active GAs into their inactive forms, thereby contributing to the manifestation of MRDD syndrome. Conversely, in resistant maize, the presence of ZmGDIα-hel dramatically inhibits the RBSDV-induced *ZmGA2ox7.3* expression and prevents ZmGA2ox7.3 oligomerization, resulting in minimal or no MRDD symptoms.

Viral effectors such as TMV replicase and RDV-P2 disrupt plant hormone balance[19,34]. In the current study, the RBSDV P7-1 effector not only stimulates *ZmGA2ox7.3* expression but also amplifies its enzymatic activity when combined with ZmGDIα. Therefore, P7-1 plays a vital role in promoting ZmGA2ox7.3 to reduce GA_1 and GA_4 levels. Notably, in a previous Co-IP/MS assay, we identified seven auxin response factors (ARFs) (Supplemental Table 2). Given that ARFs act as transcriptional activators in the auxin signaling pathway, our findings hint at the possibility that the ZmGDIα/P7-1 complex might also interface with these ARFs, thereby potentially disrupting the auxin balance.

Methods

Plant materials

A pair of near-isogenic lines (NILs), namely NIL-S and NIL-R, were derived from our previous study[5]. NIL-R carries the resistance gene *ZmGDIα-hel*, while NIL-S carries the susceptibility gene *ZmGDIα*. Transgenic plants (*ZmGA2ox7.3-GFP*-OE and *P7-1-GFP*-OE) were generated in the Maize Functional Genomic Project of China Agricultural University, using the susceptible maize inbred line B73 as the recipient.

Artificial inoculation of RBSDV

Maize kernels were germinated in vermiculite soil in pots in a greenhouse. The seedlings were artificially inoculated by either viruliferous planthoppers carrying RBSDV or non-viruliferous planthoppers without RBSDV during the emergence stage for a duration of 3 days[35]. After inoculation, the seedlings were transplanted into the field. The detailed methodology was described in our previous study[5].

Cytological and histological examination

Seedlings of the NILs were artificially infested with viruliferous planthoppers. At 60 days post-inoculation (dpi), the uppermost internodes of both NIL-S and NIL-R were sampled by cutting discs with a thickness of less than 1 mm. These samples were then immersed in a 2.5% glutaraldehyde stationary solution (Huayueyang Biotechnology, China) overnight at 4 °C. The samples then underwent a series of five processing steps, including fixation, post-fixation, dehydration, embedding, and sectioning, following the methodology outlined in the previous study[36]. Eventually, images of the samples were captured using Tecnai G2 spirit BioTwin (FEI, USA).

The transgenic ZmGA2ox7.3-GFP-OE and the recipient B73 plants were grown until anthesis, at which point the uppermost internodes were sampled and immobilized using the same procedures as described above. The samples were washed three times with PBS buffer, followed by a 2-h treatment with 1% OsO4 in PBS buffer (136.8 mM NaCl, 2.7 mM KCl, 4 mM Na_2HPO4, 1.8 mM KH_2PO4). They were then washed an additional three times with PBS. The samples underwent a series of ethanol dehydration steps at concentrations of 30%, 50%, 70%, 80%, 90% and 100%, with two subsequent rounds using 100% ethanol. Afterwards, the samples were further dehydrated in an automatic critical point dryer (Leica EM CPD 00, Germany). Ultimately, the samples were coated with a layer of gold and photographed using a S-3400N Hitachi scanning electron microscope (Hitachi Hi-Tech, Tokyo, Japan).

RNA extraction, RT-qPCR and RNA-seq

Total RNA was extracted from maize leaves or internodes with a PLANTpure plant RNA Kit (Aidlab, China), following the manufacturer's protocol. Reverse transcription was performed using *TransScript*® RT/RI reverse transcriptase with random primers (Transgen Biotech, China), according to the manufacturer's protocol. The full-length cDNA sequence of *ZmGA2ox7.3* was amplified from the two NILs. RT-qPCR assays were performed on a CFX Connect real-time RT-PCR system (BIO-RAD, USA) using a SYBR Green qRT-PCR kit (Takara, Japan) to detect the expression levels of specific genes. The primer pairs qZmGA2ox, qP7-1, qZmDAO, qZmPP1 and qZmB1B2 were used to quantify the transcript levels of *ZmGA2ox7.3*, *RBSDV-S7-1*, *ZmDAO1*, *ZmPP1* and *ZmB1B2* respectively (Supplementary Data 1). The expression level of *ZmTubulin* was used as an internal control to calculate the relative expression levels of other genes using the $2^{-\Delta\Delta Ct}$ method.

RNA-seq was performed by Novogene Bioinformatics Technology (Beijing, China). The purity and integrity of the extracted RNA samples were evaluated using a Nanodrop spectrophotometer and an Agilent 2100 Bioanalyzer, respectively. The libraries were constructed and sequenced on an Illumina Hiseq platform, generating 125 bp/150 bp paired-end reads. The raw data (raw reads) in FASTQ format were subjected to quality control, with the removal of adaptor sequences and low-quality reads to get clean reads. These clean reads were then aligned to the Maize genome (B73 RefGen_v4, AGPv4) using HISAT (2.0.4) with default parameters. FPKM (fragments per kilobase of transcript per million mapped reads) values of each gene were calculated using HTSeq (version 0.6.1) software. Differentially expressed genes (DEGs) were analyzed using DESeq (1.12.0) software, with significant DEGs defined based on a *P*-value threshold (log2 fold change > 1, $P < 0.05$). The z-score scale represents the mean-subtracted, regularized log-transformed FPKM values. The abundance of reads was visualized using the Integrative Genomics Viewer (2.16.1). Gene ontology (GO) enrichment analysis was performed using the accession numbers of significant DEGs via GOseq (version 2.12). Pathway enrichment analysis of DEGs was conducted using KOBAS (version 2.0). The RNA-seq analysis included two independent biological replicates, with the whole uppermost leaves harvested from at least five individual plants for each sample.

Construct generation and plant transformation

The primer sequences used in this study are listed in Supplementary Data 1. All constructs were generated using the homologous recombination cloning system (Yeasen Biotechnology, China). Sequencing was performed to confirm the absence of mutations in the PCR fragments that were inserted into vectors. For the generation of *ZmGA2ox7.3-GFP*, *ZmGA2ox7.3-mCherry*, and *ZmGA2ox7.3-Myc* constructs, the coding sequence (CDS) of *ZmGA2ox7.3* was amplified and cloned into the Super1300-GFP, Super1300-Myc, and Super1300-mCherry vectors, respectively. Likewise, both the full-length and fragmentary coding sequences of *ZmGDIα* and *ZmGDIα-hel* were inserted into the Super1300-Myc vector.

To generate SLC constructs, we amplified the coding sequences (CDSs) of *ZmGA2ox7.3*, *ZmGDIα*, and *ZmGDIα-he*l and subsequently cloned them into JW771-35S-NLuc and JW772-35S-CLuc vectors. A series of fragments from the *ZmGDIα* and *ZmGDIα-hel* genes were also amplified and inserted into JW772-35S-CLuc to fuse with the C-terminal fragment of the luciferase gene (cLUC) as described previously[5].

To generate the *GST-ZmGA2ox7.3*, *His-ZmGA2ox7.3*, *His-ZmGDIα*, and *His-ZmGDIα-hel* constructs, the CDSs were cloned into the pGEX6P-1, pCold-TF, and PHAT2 vectors, respectively. The $ZmGA2ox7.3^{C198A/K312A/R317A}$ (*GST-ZmGA2ox7.3*^{3A}) construct was performed by ClonExpress MultiS One Step Kit (Vazyme, China).

To generate transgenic maize and Arabidopsis thaliana plants, the CDSs of *RBSDV-S7-1*and *ZmGA2ox7.3*^{3A} were amplified and cloned into the Super1300-GFP vector, respectively. Using the *pSuper:RBSDV-S7-1-GFP* and *pSuper:ZmGA2ox7.3-GFP* constructs as templates, we amplified fragments of *RBSDV-S7-1-GFP* and *ZmGA2ox7.3-GFP*, which were then inserted into the pBCXUN vector to generate the *pUbi:ZmGA2ox7.3-GFP* and *pUbi:RBSDV-P7-1-GFP* constructs, respectively.

The cDNA of *ZmGA2ox7.3* was cloned into the P2YC or P2YN vector to generate *cYFP-ZmGA2ox7.3/nYFP-ZmGA2ox7.3* constructs. The full-length sequences of *RBSDV-S7-1*, *ZmGDIα/ZmGDIα-hel*, *ZmDAO1*, *ZmB1B2*, *ZmPP1*, as well as truncated versions of *ZmGDIα/ZmGDIα-hel*, also were cloned into the P2YN or P2YC vectors. This resulted in the generation of the following constructs: *nYFP-P7-1*, *nYFP-ZmDAO1*, *nYFP-ZmB1B2*, *nYFP-ZmPP1*, *nYFP-ZmGDIα/cYFP-ZmGDIα*, *nYFP-ZmGDIα-hel/cYFP-ZmGDIα-hel*, *nYFP-ZmGDIα*$^{1\text{-}146}$, *nYFP-ZmGDIα*$^{146\text{-}333}$, *nYFP-ZmGDIα-hel*$^{146\text{-}319}$, and *nYFP-ZmGDIα*$^{379\text{-}445}$, respectively.

To generate *LUC* constructs, a 3.0 kb promoter fragment of *ZmGA2ox7.3* was amplified and inserted into the *pGreenII0800-LUC* vector to generate the *pZmGA2ox7.3:LUC* construct. The 13 *RBSDV* sequences were cloned into the *pGreenII62-SK* vector to generate the 13 effector vectors. The P7-1-myc, P7-1-nLUC, MBP-P7-1, and pCold-TF-His-P7-1 constructs were obtained from our previous study[5].

Subcellular localization

To detect the subcellular localization of the ZmGA2ox7.3 protein, the *pSuper: ZmGA2ox7.3-GFP*, *pSuper1300-GFP*, and *35S:PIP2A-mCherry* (a plasma membrane protein) constructs were transformed into *Agrobacterium* strain EHA105. After an overnight culture in LB media at 28 °C, equal volumes of *Agrobacterium* cultures, normalized to an OD600 value, were harvested for the GFP and mCherry constructs. These cultures were then resuspended in infiltration buffer (10 mM $MgCl_2$, 10 mM MES, 150 mM acetosyringone, pH 5.8) and incubated for 2 h at 28 °C. Subsequently, the suspensions were infiltrated into leaves of three-week-old *N. benthamiana*, and the fluorescence signals were visualized two days post-infiltration. Additionally, the *pSuper:ZmGA2ox7.3-mCherry* and *pSuper:mCherry* constructs were also transformed into maize protoplasts and incubated at 28 °C for 12 h. The GFP and mCherry fluorescence signals were visualized using confocal laser scanning microscopy (ZEISS880, Carl Zeiss) after 72 h of transformation.

Phylogenetic analysis

The amino acid sequences of GA2ox from maize and rice were downloaded from the National Center for Biotechnology Information (https://www.ncbi.nlm.nih.gov/) and the maize database (https://www.maizegdb.org/), respectively. The phylogenetic tree was constructed using the neighbor-joining method with MEGA7.0 software (https://www.megasoftware.net/).

Split luciferase complementation (SLC) assay

The resulting constructs were transformed into *Agrobacterium* EHA105 and co-infiltrated into *N. benthamiana* leaves as previously described. 72 h after transformation, the initial infiltration sites were injected with 1 mmol/L beetle luciferase (Promega, USA). The chemiluminescent signal was then captured using the Chemiluminescent Imaging System (Tanon, China). Additionally, to further assess the chemiluminescent signal, the infiltrated sites were injected with 0.5 mM GA_4.

Total protein was extracted from the injected leaves using laemmli sample buffer (0.125 M Tris-HCl, 4% SDS, 20% glycerol, 10% 2-mercaptoethanol, 0.004% bromophenol blue, pH 6.8). The resulting supernatants were subjected to immunoblotting with an α-LUC antibody (Abcam, UK) and a plant-specific actin antibody (ABclonal Technology, China). The fluorescence signals and immunoblot bands were quantified for their intensities using ImageJ Launcher software (National Institutes of Health), and the measurements were expressed as mean gray value.

Co-immunoprecipitation (Co-IP) assay

The relevant constructs were co-expressed in *N. benthamiana* leaves through co-infiltration for 72 h. Total protein was then extracted from the infiltrated leaves using IP buffer (50 mM Tris-MES, 10 mM EDTA, 0.5 M sucrose, 1 mM $MgCl_2$, 5 mM DTT, 1 mM PMSF, pH 8.0). The extracted supernatants were incubated with anti-GFP magnetic beads (MBL, China) for 2 h, after which the beads were washed three times with IP buffer. The immunoprecipitated complexes were heated in SDS loading buffer (Genstar, China) at 100 °C for 5 min and subsequently subjected to immunoblotting using an anti-Myc antibody (MBL, China).

Pull-down assays

The relevant fusion constructs were transformed into *Escherichia coli* strain BL21 (DE3) (TransGen Biotech, China). The recombinant GST-ZmGA2ox7.3, His-ZmGDIα, His-ZmGDIα-hel, and His-P7-1 proteins were subsequently purified using affinity chromatography. GST-fused proteins were purified using glutathione sepharose (Yeasen, China), while His-fused proteins were purified using Ni Sepharose (GE Healthcare, USA), all according to the manufacturers' instructions. GST or GST-ZmGA2ox7.3 was immobilized on glutathione agarose beads and incubated at 4 °C for 1 h. These immobilized proteins were then incubated with His-ZmGDIα, His-ZmGDIα-hel, and His-P7-1 for an additional 2 h. Following elution from the beads, the proteins were subjected to immunoblotting using an anti-His antibody (Easybio, China).

Bimolecular fluorescence complementation (BiFC) assay

The relevant constructs were transformed into *Agrobacterium* EHA105 and were co-infiltrated into *N. benthamiana* leaves and allowed to express for 72 h. GFP fluorescence was visualized using confocal microscopy (ZEISS880, Carl Zeiss) with an excitation wavelength set at 488 nm. For the combinations involving *nYFP-ZmGA2ox7.3* and *cYFP-ZmGA2ox7.3*, the infiltrated sites were treated with either 0.1% Tween 20 or 0.1% Tween 20 with 0.5 mM GA_4. Subsequently, the GFP fluorescence signals were assessed. The fluorescence intensities were quantified using ZEN software.

Microscale Thermophoresis (MST) Assay

The purified proteins, GST-ZmGA2ox7.3, His-P7-1, His-ZmGDIα, and His-ZmGDIα-hel, were concentrated and dialyzed in PBS buffer (pH 7.4) using an Amicon Ultra-4 concentrator unit with a 10 kDa molecular weight cutoff (Millipore, USA). To investigate the strength of interaction between ZmGA2ox7.3 and P7-1, ZmGDIα or ZmGDIα-hel, the MST assays were subjected to performed according to the manufacturer's instructions (Nano Temper Technologies, Cat# MO-L011). The binding reactions were measured by using a microscale thermophoresis instrument (Nano Temper Technologies) at 25 °C, 40% MST power and 20% LED power. The Nano Temper Analysis Software MO affinity Analysis was used to calculate the value of the dissociation constant (Kd).

Transient expression assays in maize protoplasts

For dual-luciferase assays, the *pZmGA2ox7.3:LUC* construct served as the reporter gene, while the *62SK-RBSDVs* and *35S:S7-1-GFP* constructs, driven by the 35S promoter, acted as effectors. The REN gene, under the control of the 35S promoter, was included in the *pGreenII0800-LUC* vector as an internal control. Empty effectors *pGreenII 62-SK* and *35:GFP* were employed as controls. Appropriate combinations of reporter and effector constructs were co-transformed into maize protoplasts and incubated at 28 °C for 12 h. Luciferase signals were detected according to the instructions of the Dual-Luciferase Reporter Assay System (Promega, USA). The ratio of REN activity to LUC activity was taken as the relative LUC activity. Each experiment was performed with at least three biological replicates.

Gel filtration chromatography analysis

Standard curves correlating elution volume to molecular weight were generated according to the manufacturer's instructions (GE Healthcare, USA). The mixture, containing ~3 mg of each standard protein, was injected onto a Superdex™ 200 Increase 10/300 GL column (GE Healthcare, USA). The standard proteins were added in the following order: thyroglobulin (669 kDa), ferritin (450 kDa), aldolase (158 kDa), conalbumin (75 kDa), and ovalbumin (42 kDa). Blue Dextran 2000 was used to define the column void volume (V_o). The mobile phase consisted of 0.01 M phosphate buffer saline at pH 7.4, and the flow rate was set to 0.3 ml/min. A standard curve for Kav and Mr was constructed based on the formula $K_{av} = (V_e\text{-}V_o)/(V_c\text{-}V_o) = a\text{-}b*\log_{10}(Mr)$, where V_c represents the column volume, V_e is the elution volume, and Mr denotes the protein molecular weight, using data obtained from the standard proteins.

The purified proteins, GST-ZmGA2ox7.3, GST-ZmGA2ox7.3^{3A}, MBP-P7-1, His-ZmGDIα, and His-ZmGDIα-hel, were concentrated and dialyzed in PBS buffer (pH 7.4) using an Amicon Ultra-4 concentrator unit with a 10 kDa molecular weight cutoff (Millipore, USA). These proteins were then incubated at 25 °C for 12 h in PBS

buffer containing 10 mM GA_4, using ethanol as the control. After incubation, the proteins were centrifuged at high speed for 10 min and fractionated through size exclusion chromatography. The chromatography was executed using an AKTA Purifier System (Cytiva, USA) equipped with a Superdex 200 Increase 10/300 GL column. The system, equilibrated with PBS buffer, eluted samples with the same buffer at a flow rate of 0.3 ml/min at 4 °C. Eluted fractions (0.5 ml each) were continuously collected, and peak fractions were subjected to 4–13% Blue Native-PAGE and 10% SDS-PAGE, followed by immunoblotting with an anti-GST antibody.

Blue native polyacrylamide gel electrophoresis (BN-PAGE)

To investigate the oligomerization of ZmGA2ox7.3, the peak fractions were subjected to 4–13% Blue Native PAGE (WSHTBio, China) according to the manufacturer's instructions. The resolved samples were then transferred onto polyvinylidene difluoride (PVDF) membranes using a methanol-free transfer buffer (48 mM Tris-base, 39 mM glycine), followed by immunoblotting using the appropriate antibodies.

Enzyme activity assay

For the enzymatic activity assay, we adopted specific procedures from a prior study[27]. The purified proteins GST-ZmGA2ox7.3, MBP-P7-1, His-ZmGDIα, and His-ZmGDIα-hel were each incubated in 1 ml of enzymatic activity buffer (100 mM Tris-HCl, 4 mM ascorbic acid, 4 mM 2-oxoglutaric acid, 0.5 mM FeSO4, 4 mM DTT, 2 mg/ml BSA, and 1 mg/ml catalase, pH 7.9). The mixture was then incubated with 0.5 mM GA_4 at 30 °C for 12 h. To terminate the reaction, 125 µl of acetic acid was added to each solution, and the mixture was kept at 30 °C for an additional hour. The level of the enzyme reaction product, GA_{34}, was subsequently quantified by Wuhan Greensword Creation Technology Co. Ltd. (http://www.greenswordcreation.com). Each experiment was conducted with three biological replicates.

Mass Spectrometry (MS)

The elution fractions were analyzed by mass spectrometry (MS) at the Biological Mass Spectrum Laboratory, College of Biological Sciences, China Agricultural University. The elution fractions from the two "Mu" peaks were collected and separated by BN-PAGE as described. The gel lanes were excised, sliced, subjected to in-gel digestion with trypsin, and redissolved in trifluoroacetic acid, following the methodology outlined in a previous study[37]. The extracted peptides were then analyzed using an LTQ Orbitrap Velos mass spectrometer (Thermo Fisher Scientific). Protein identification was performed using the Mascot search engine (Mascot Server 2.3, Matrix Science) by blasting with the UniProt protein database (https://www.uniprot.org/). In the previous study, the false discovery rate (FDR) and significance threshold have been set[37].

Transgenic tests in Arabidopsis thaliana

The *pSuper1300:ZmGA29X7.3-GFP* and *pSuper:ZmGA2ox7.3*^{3A}*-GFP* constructs were transformed into Col-0 to obtain OE-ZmGA2ox7.3^{3A} (OE^{3A}–1 and OE^{3A}–2), and OE-ZmGA2ox7.3 (OE-1 and OE-2) transgenic plants, respectively. Stable T_2 generation of four above lines were used for experiments.

Measurement of plant hormones

NIL-S and NIL-R were both artificially infested with planthoppers, either carrying RBSDV or not. Subsequently, the uppermost internodes and upper leaves were sampled at 60 dpi. The collected samples were used to measure the content of various endogenous phytohormones, including gibberellins (Gas), indole-3-acetic acid (IAA), and cytokinins (CKs). The quantification of these phytohormones was executed using UHPLC-MS/MS analysis (Thermo Scientific Ultimate 3000 UHPLC coupled with TSQ Quantiva). This analysis was conducted by Wuhan Greensword Creation Technology Co. Ltd. (http://www.greenswordcreation.com) according to established methods[38]. The experiments were conducted with three biological replicates.

Application of exogenous GAs

Exogenous GA_3 and GA_4 treatments were performed following previously described methods[39]. Seeds from both the recipient B73 and *ZmGA2ox7.3-GFP*-OE transgenic lines were germinated in pots filled with vermiculite soil and placed in a greenhouse. They were kept under conditions of 26 °C with a 16-h white light/8-h dark cycle for 6 days. Subsequently, the entire plants were uniformly sprayed with either GA_1 (100 µg·ml^{-1}, 0.1% Tween-20), GA_3 (1 mg·ml^{-1}, 0.1% Tween-20), GA_4 (100 µg·ml^{-1}, 0.1% Tween-20) or 0.1% Tween-20 (as a control). Plants heights were measured 8 days post-treatment. Both the transgenic lines and the control plants were represented by at least three biological replicates.

Quantification and statistics analysis

Statistical parameters are reported in the figures and figure legends. Statistical analyses were preformed using GraphPad Prism 8.3.0. Data were tested for normality using the Shapiro-Wilk normality test in GraphPad Prism 8.3.0. For normally distributed data, statistical significane between two groups was assessed using a two-tailed student's *t* test or LSD's *t* test. For comparisons among more than two groups, one-way ANOVA with Tukey's test or LSD's *t*-test was used, and different lowercase letters indicate a significant difference ($P < 0.05$). For data that were not normally distributed, the Mann-Whitney U test or Wilcoxon matched-pairs signed-rank test were used for two-group comparisons, while the Kruskal-Wallis test was employed for comparisons among more than two groups. Different lowercase letters indicate a significant difference ($P < 0.05$). The Pearson's correlation coefficient (R) and *P* values were calculated using GraphPad Prism 8.3.0. All statistics analyses in this study were conducted using GraphPad Prism 8.3.0.

Reporting summary

Further information on research design is available in the Nature Portfolio Reporting Summary linked to this article.

Data availability

The authors declare that the data supporting the findings of this study are available within the paper and its supplementary files. A reporting summary for this paper is available as a supplementary file. The raw data of RNA-Seq are available from NCBI (National Center for Biotechnology Information) website under primary GEO accessions number GSM7948644 - GSM79486447 (https://www.ncbi.nlm.nih.gov/gds/?term=GSM7948644; https://www.ncbi.nlm.nih.gov/gds/?term=GSM7948645; https://www.ncbi.nlm.nih.gov/gds/?term=GSM7948646; https://www.ncbi.nlm.nih.gov/gds/?term=GSM7948647). The datasets generated and analyzed during this study are provided in the Supplementary information and Source Data file. Source data are provided with this paper.

References

1. Gao, D. M. et al. A plant cytorhabdovirus modulates locomotor activity of insect vectors to enhance virus transmission. *Nat. Commun.* **14**, 5754 (2023).
2. Nicaise, V. Crop immunity against viruses: outcomes and future challenges. *Front. Plant Sci.* **5**, 660 (2014).
3. Truniger, V. & Aranda, M. A. Recessive resistance to plant viruses. *Adv. Virus Res.* **75**, 119–159 (2009).
4. Hashimoto, M., Neriya, Y., Yamaji, Y. & Namba, S. Recessive resistance to plant viruses: potential resistance genes beyond translation initiation factors. *Front. Microbiol.* **7**, 1695 (2016).

5. Liu, Q. et al. A helitron-induced RabGDIα variant causes quantitative recessive resistance to maize rough dwarf disease. *Nat. Commun.* **11**, 495 (2020).
6. Ouibrahim, L. et al. Cloning of the Arabidopsis rwm1 gene for resistance to Watermelon mosaic virus points to a new function for natural virus resistance genes. *Plant J.* **79**, 705–716 (2014).
7. Yang, P. et al. PROTEIN DISULFIDE ISOMERASE LIKE 5-1 is a susceptibility factor to plant viruses. *Proc. Natl Acad. Sci. USA* **111**, 2104–2109 (2014).
8. Harpaz, I. Needle transmission of a new maize virus. *Nature* **184**, 77–78 (1959).
9. Milne, R. G. & Lovisolo, O. Maize rough dwarf and related viruses. *Adv. Virus Res.* **21**, 267–341 (1977).
10. Distéfano, A. J. et al. Sequence analysis of genome segments S4 and S8 of Mal de Río Cuarto virus (MRCV): evidence that the virus should be a separate Fijivirus species. *Arch. Virol.* **9**, 1699–1709 (2002).
11. Uyeda, I., Kimura, I. & Shikata, E. Characterization of genome structure and establishment of vector cell lines for plant reoviruses. *Adv. Virus Res.* **45**, 249–279 (1995).
12. Shen, J., Chen, X., Chen, J. & Sun, L. A phloem-limited fijivirus induces the formation of neoplastic phloem tissues that house virus multiplication in the host plant. *Sci. Rep.* **6**, 29848 (2016).
13. Zhang, H. M., Chen, J. P. & Adams, M. J. Molecular characterisation of segments 1 to 6 of Rice black-streaked dwarf virus from China provides the complete genome. *Arch. Virol.* **146**, 2331–2339 (2001).
14. Li, M. et al. Maize AKINβγ proteins interact with P8 of rice black streaked dwarf virus and inhibit viral infection. *Viruses* **12**, 1387 (2020).
15. Isogai, M., Uyeda, I. & Lee, B. C. Detection and assignment of proteins encoded by rice black streaked dwarf fijivirus S7, S8, S9 and S10. *J. Gen. Virol.* **79**, 1487–1494 (1998).
16. Sun, Z. et al. The secretory pathway and the actomyosin motility system are required for plasmodesmatal localization of the P7-1 of rice black-streaked dwarf virus. *Arch. Virol.* **158**, 1055–1064 (2013).
17. Alazem, M. & Lin, N. S. Roles of plant hormones in the regulation of host-virus interactions. *Mol. Plant Pathol.* **16**, 529–540 (2015).
18. Zhao, S. & Li, Y. Current understanding of the interplays between host hormones and plant viral infections. *PLoS Pathog.* **17**, e1009242 (2021).
19. Padmanabhan, M. S., Goregaoker, S. P., Golem, S., Shiferaw, H. & Culver, J. N. Interaction of the tobacco mosaic virus replicase protein with the Aux/IAA protein PAP1/IAA26 is associated with disease development. *J. Virol.* **79**, 2549–2558 (2005).
20. Zhu, S. et al. The rice dwarf virus P2 protein interacts with ent-kaurene oxidases in vivo, leading to reduced biosynthesis of gibberellins and rice dwarf symptoms. *Plant Physiol.* **139**, 1935–1945 (2005).
21. Zhang, H. et al. Different viral effectors suppress hormone-mediated antiviral immunity of rice coordinated by OsNPR1. *Nat. Commun.* **14**, 3011 (2023).
22. Baliji, S., Lacatus, G. & Sunter, G. The interaction between geminivirus pathogenicity proteins and adenosine kinase leads to increased expression of primary cytokinin-responsive genes. *Virology* **402**, 238–247 (2010).
23. Huang, S. et al. A plant NLR receptor employs ABA central regulator PP2C-SnRK2 to activate antiviral immunity. *Nat. Commun.* **15**, 3205 (2024).
24. Olszewski, N., Sun, T. P. & Gubler, F. Gibberellin signaling: biosynthesis, catabolism, and response pathways. *Plant Cell* **14**, S61–S80 (2002).
25. He, J. et al. CYP72A enzymes catalyse 13-hydrolyzation of gibberellins. *Nat. Plants* **5**, 1057–1065 (2019).
26. Yamaguchi, S. Gibberellin metabolism and its regulation. *Annu Rev. Plant Biol.* **59**, 225–251 (2008).
27. Takehara, S. et al. A common allosteric mechanism regulates homeostatic inactivation of auxin and gibberellin. *Nat. Commun.* **11**, 2143 (2020).
28. Schomburg, F. M., Bizzell, C. M., Lee, D. J., Zeevaart, J. A. & Amasino, R. M. Overexpression of a novel class of gibberellin 2-oxidases decreases gibberellin levels and creates dwarf plants. *Plant cell* **15**, 151–163 (2003).
29. Liu, C. et al. Shortened basal internodes encodes a Gibberellin 2-Oxidase and contributes to lodging resistance in rice. *Mol. Plant* **11**, 288–299 (2018).
30. Jiang, T. et al. Activated malate circulation contributes to the manifestation of light-dependent mosaic symptoms. *Cell Rep.* **42**, 112333 (2023).
31. Zhang, H. et al. Distinct modes of manipulation of rice auxin response factor OsARF17 by different plant RNA viruses for infection. *Proc. Natl Acad. Sci. USA* **117**, 9112–9121 (2020).
32. Bolduc, N. & Hake, S. The maize transcription factor KNOTTED1 directly regulates the gibberellin catabolism gene ga2ox1. *Plant Cell* **21**, 1647–1658 (2009).
33. Wang, H., Caruso, L. V., Downie, A. B. & Perry, S. E. The embryo MADS domain protein AGAMOUS-Like 15 directly regulates expression of a gene encoding an enzyme involved in gibberellin metabolism. *Plant Cell* **16**, 1206–1219 (2004).
34. Jin, L. et al. Rice dwarf virus P2 protein hijacks auxin signaling by directly targeting the rice OsIAA10 protein, enhancing viral infection and disease development. *PLoS Pathog.* **12**, e1005847 (2016).
35. Abendroth, L. J., Elmore, R. W., Boyer, M. J. & Marlay, S. K. *Corn Growth and Development* (Iowa State University, Ames, Iowa, 2011).
36. Hülskamp, M., Schwab, B., Grini, P. & Schwarz, H. Transmission electron microscopy (TEM) of plant tissues. *Cold Spring Harb. Protoc.* **2010**, pdb.prot4958 (2010).
37. Zhong, T. et al. The ZmWAKL-ZmWIK-ZmBLK1-ZmRBOH4 module provides quantitative resistance to gray leaf spot in maize. *Nat. Genet.* **2**, 315–326 (2024).
38. Chen, M. L. et al. Highly sensitive and quantitative profiling of acidic phytohormones using derivatization approach coupled with nano-LC-ESI-Q-TOF-MS analysis. *J. Chromatogr. B Anal. Technol. Biomed. Life Sci.* **905**, 67–74 (2012).
39. Chen, Z. et al. Development of dwarfish and yield-effective GM maize through passivation of bioactive gibberellin. *Transgenic Res.* **28**, 589–599 (2019).

Acknowledgements

We would like to extend our gratitude to all members of the Xu laboratory for their insightful discussions and technical support. We appreciate the Center for Crop Functional Genomics and Molecular Breeding of China Agricultural University for providing transgenic technology support. Our thanks also go to the Public Instrument Platform of Collegue of Agronomy and Biotechnology. China Agricultural University, for assistance with Confocal Microscopy and Gel Filtration Chromatography. We are grateful to Drs. Peisi Wang (Nanjing Agricultural University), Shengfeng He (China Agricultural University), and Mingzhu Yan (China Agricultural University) for kindly providing BiFC vectors and transient expression-based systems. This project was supported by National Key Research and Development Program (Grant No: 2022YFD1201800, M.X.) and the China Postdoctoral Science Foundation (Grant No: 2023M733808, S.D.).

Author contributions

M.X. and S.D. conceived the research and designed the experiments. M.X. supervised the project. S.D. performed most of the experiments. S.J. was involved in protein interaction assays. B.L. provided the materials and supported artificial inoculation in the field. T.Z. helped revise the manuscript and the charts. Q. L., J.L., and Y.L. also participated in both the artificial inoculation and phenotypic evaluation in the field. C.Y.

and C.S. contributed to confocal microscopy and gel filtration chromatography. M.X. and S.D. wrote the manuscript, with contributions and feedback from all authors.

Competing interests
The authors declare no competing interests.

Additional information
Supplementary information The online version contains supplementary material available at https://doi.org/10.1038/s41467-024-51726-7.

Correspondence and requests for materials should be addressed to Mingliang Xu.

Peer review information *Nature Communications* thanks Tong Zhang, and the other, anonymous, reviewer(s) for their contribution to the peer review of this work. A peer review file is available.